Journal of Power Sources 213 (2012) 16–30

Contents lists available at SciVerse ScienceDirect

Journal of Power Sources

journal homepage: www.elsevier.com/locate/jpowsour

# Alkaline membrane fuel cell (AMFC) modeling and experimental validation

E.M. Sommer [a,b], L.S. Martins [b], J.V.C. Vargas [a,*], J.E.F.C. Gardolinski [c], J.C. Ordonez [b], C.E.B. Marino [a]

[a] Departamento de Engenharia Mecânica, Universidade Federal do Paraná, C. P. 19011, Curitiba, Paraná 81531-990, Brazil
[b] Department of Mechanical Engineering and Center for Advanced Power Systems, Florida State University, Tallahassee, FL 32310-6046, USA
[c] PANalytical B.V., Lelyweg 1, 7602EA, Almelo, The Netherlands

ARTICLE INFO

*Article history:*
Received 3 March 2012
Received in revised form
22 March 2012
Accepted 23 March 2012
Available online 11 April 2012

*Keywords:*
Alkaline membrane fuel cell
Potassium hydroxide
Dynamic mathematical modeling
Experimental validation

ABSTRACT

This paper aims to produce a dynamic model that is computationally fast to predict the response of the single AMFC according to variations of physical properties of the materials, and operating and design parameters. The model is based on electrochemical principles, and mass, momentum, energy and species conservation. It also takes into account pressure drop in the gas channels and the temperature gradient with respect to space in the flow direction. The simulation results comprise temperature distribution, net power and polarization curves, which were experimentally validated by direct comparison to voltage and current measurements performed in a cellulose-based AMFC prototype for different electrolyte (KOH) solution concentrations (y), showing good quantitative and qualitative agreement. It is concluded that the startup transient is short and that there are optimal values of y (~40 wt. %) which lead to maximum power, that are herein shown experimentally for the first time. In the process, the model was used to formulate empirical correlations for the exchange current density ($i_0$) in the electrodes with respect to the electrolyte concentration for future fuel cell development. Therefore, the adjusted and validated model is expected to be a useful tool for AMFC control, design and optimization purposes.



## 1. Introduction

Fuel cell technology is currently at an advanced stage. However, there are still challenging hurdles to be overcome to allow for extensive utilization, such as improvements on hydrogen production, storage and distribution, catalysts cost reduction and manufacturing [1,2].

Among the existing fuel cell types [2], Alkaline Fuel Cells (AFC) have interesting features as compared to polymer electrolyte fuel cells (PEMFC), such as higher current density, lower cost electrolyte (KOH aqueous solution) and mainly, the possibility of using non-noble catalysts (e.g., nickel, silver), since faster kinetics of the reactions is observed in alkaline media than in acid media [3,4]. Additionally, AFC can work at higher temperatures (100–120 °C) than PEMFC, which cannot operate above 90 °C due to the need to hydrate the nafion membrane [4]. However, PEMFC are more suitable for vehicular applications mainly due to the use of solid electrolytes that eliminate the risk of leakage [2].

The electrolyte in the AFC consists of an aqueous alkaline solution, such as potassium hydroxide (KOH). Since aqueous alkaline solutions absorb carbon dioxide ($CO_2$), an undesirable "poisoning" effect is observed through the conversion of KOH to potassium carbonate ($K_2CO_3$), in a reaction that competes with the expected redox reaction between hydrogen and oxygen at the anode and cathode [4]. This reaction has the effect of reducing the number of hydroxyl ions available for reaction at the electrodes, also reducing the ionic conductivity of the electrolyte solution, and could block the pores of the gas diffusion layer (GDL) by the precipitation of $K_2CO_3$ salt, but not causing any degradation of the electrodes [5]. As a result, the AFC performance is greatly reduced in air breathing systems, i.e., when the oxidant is air which contains $CO_2$.

Because of the $CO_2$ poisoning effect, alkaline fuel cells typically operate on pure-oxygen, or at least purified air, and must have built-in mechanisms to clean out as much of the carbon dioxide as is possible. Because the generation and storage requirements of oxygen make pure-oxygen AFCs expensive, the active development of the technology has not attracted large industrial interest. Although the harmful effects of carbon dioxide poisoning can be partly reduced by several different strategies [4], a permanent solution would increase the possibility of AFC commercialization.

In order to cope with that reality, two types of AFCs exist: static electrolyte and flowing electrolyte. Static, or immobilized, electrolyte cells are of the type used in the Apollo space craft and the space shuttle, which typically use an asbestos separator saturated

* Corresponding author. Tel.: +55 41 3361 3307; fax: +55 41 3361 3129.
*E-mail addresses:* jvargas@demec.ufpr.br, vargasjvcv@gmail.com (J.V.C. Vargas).

0378-7753 
doi:10.1016/j.jpowsour.2012.03.089

**Nomenclature**

| | |
|---|---|
| $A$ | area, $m^2$ |
| $A_c$ | total gas channel cross-section area, $m^2$ |
| $A_s$ | fuel cell cross-section area, $m^2$ |
| $A_w$ | wall heat transfer area, $m^2$ |
| AFC | alkaline fuel cell |
| AMFC | alkaline membrane fuel cell |
| B | dimensionless constant |
| $B_a$ | bias limit of quantity a |
| C | constant |
| $C_i$ | concentration of oxidized and reduced states (i = O, R), mol $m^{-3}$ |
| CFD | computational fluid dynamics |
| CVi | control volume i |
| $c$ | specific heat, kmol $kg^{-1}$ $K^{-1}$ |
| $c_p$ | specific heat at constant pressure, kJ $kg^{-1}$ $K^{-1}$ |
| $D$ | Knudsen diffusion coefficient, $m^2$ $s^{-1}$ |
| $D_h$ | gas channel hydraulic diameter, m |
| $f$ | friction factor |
| $F$ | Faraday constant, 96,500 C $eq^{-1}$ |
| $h$ | heat transfer coeficient, W $m^{-2}$ $k^{-1}$ |
| $H_i(T_i)$ | molar enthalpy of formation at temperature $T_i$ of reactants and products, kJ $kmol^{-1}$ of compound i |
| $\tilde{H}_i(\theta_i)$ | dimensionless molar enthalpy of formation at temperature $\theta_i$ of reactants and products of compound i |
| IPPE | inverse problem of parameter estimation |
| $i_{o,a}$, $i_{o,c}$ | anode and cathode exchange current densities, A $m^{-2}$ |
| $i_{Lim,a}$, $i_{Lim,c}$ | anode and cathode limiting current densities, A $m^{-2}$ |
| $I$ | current, A |
| $j$ | mass flux, kg $m^2$ $s^{-1}$ |
| $k$ | thermal conductivity, W $m^{-1}$ $K^{-1}$ |
| $k^0$ | standard rate constant, $ms^{-1}$ |
| $K$ | permeability, $m^2$ |
| $L$ | control volume length, m |
| $L_c$, $L_t$ | gas channels internal dimensions, m |
| $L_x$, $L_y$, $L_z$ | fuel cell length, width and height, respectively, m |
| $m$ | mass, kg |
| $\dot{m}$ | mass flow rate, kg $s^{-1}$ |
| $M$ | molecular weight, kg $kmol^{-1}$ |
| $n$ | equivalent electron per mole of reactant, eq $mol^{-1}$ |
| $\dot{n}$ | molar flow rate, mol $s^{-1}$ |
| $N$ | dimensionless global wall heat transfer coefficient |
| $n_c$ | number of parallel ducts in gas channel |
| $p$ | pressure, N $m^{-2}$ |
| $P$ | dimensionless pressure |
| $P_a$ | precision limit of quantity a |
| $p_s$ | perimeter of cross-section, m |
| PEMFC | proton exchange membrane fuel cell |
| $Pr$ | Prandtl number, $\mu c_p/k$ |
| $q$ | tortuosity |
| $Q$ | reaction quotient |
| $\dot{Q}$ | heat transfer rate, W |
| $r$ | pore radius, m |
| $R$ | ideal gas constant, kJ $kg^{-1}$ $K^{-1}$ |
| $\overline{R}$ | universal gas constant, 8.314 kJ $kmol^{-1}$ $K^{-1}$ |
| $Re_{D_h}$ | Reynolds number based on $D_h$, $uD_h\rho/\mu$ |
| $t$ | time, s |
| $T$ | temperature, K |
| $u$ | mean velocity, $ms^{-1}$ |
| $U$ | global wall heat transfer coefficient, W $m^{-2}$ $K^{-1}$ |
| $U_a$ | uncertainty of quantity a |
| $V$ | electrical potential, V |
| $V_T$ | total volume, $m^3$ |
| $y$ | electrolyte solution mass fraction, wt. % |
| $W$ | electrical work, J |
| $\dot{W}$ | electrical power, W |
| $\tilde{W}$ | dimensionless fuel cell electrical power |
| $\tilde{W}_{net}$ | dimensionless fuel cell net power |
| $\tilde{W}_p$ | dimensionless required pumping power |
| $[\cdot]$ | molar concentration of a substance (mol $l^{-1}$) |

*Greek Symbols*

| | |
|---|---|
| $\alpha$ | charge transfer coefficient |
| $\beta$ | electrical resistance, Ω |
| $\gamma$ | ratio of specific heats |
| $\delta$ | gas channel aspect ratio |
| $\Delta G$ | molar Gibbs free energy change, kJ $kmol^{-1}H_2$ |
| $\Delta H$ | molar enthalpy change, kJ $kmol^{-1}H_2$ |
| $\Delta P$ | dimensionless pressure drop in gas channels |
| $\Delta S$ | molar entropy change, kJ $kmol^{-1}$ |
| $\Delta T$ | temperature change, K |
| $\zeta$ | stoichiometric ratio |
| $\eta_a$, $\eta_c$ | anode and cathode charge transfer overpotentials, V |
| $\eta_{d,a}$, $\eta_{d,c}$ | anode and cathode mass diffusion overpotentials, V |
| $\eta_{ohm}$ | fuel cell total ohmic potential loss, V |
| $\theta$ | dimensionless temperature |
| $\mu$ | viscosity, kg $m^{-1}$ $s^{-1}$ |
| $\nu_i$ | reaction coefficient |
| $\xi$ | dimensionless length |
| $\rho$ | density, kg $m^{-3}$ |
| $\sigma$ | electrical conductivity, $\Omega^{-1}$ $m^{-1}$ |
| $\tau$ | dimensionless time |
| $\phi$ | porosity |
| $\psi$ | dimensionless mass flow rate |

*Subscripts*

| | |
|---|---|
| a | anode |
| (aq) | aqueous solution |
| c | channel or cathode |
| cel | solid part of electrolyte |
| dif | diffusion |
| e | reversible |
| f | fuel |
| (g) | gaseous phase |
| $H_2$ | hydrogen |
| $H_2O$ | water |
| i | substance or location in AMFC |
| i | irreversible |
| i,a | irreversible at the anode |
| i,c | irreversible at the cathode |
| j | location in AMFC |
| KOH | potassium hydroxide |
| (l) | liquid phase |
| max | maximum |
| memb | electrolyte membrane (solid and liquid parts) |
| ohm | ohmic |
| opt | optimal |
| ox | oxidant |
| $OH^-$ | hydroxide ion |
| $O_2$ | oxygen |
| ref | reference level |
| s,a | anode solid part |
| s,c | cathode solid part |
| s | solid phase |

| | | | |
|---|---|---|---|
| sol | electrolyte solution | 56 | interaction between CV5 and CV6 |
| w | wall | 67 | interaction between CV6 and CV7 |
| wet | wetted | ∞ | ambient |
| 0 | initial condition | | |
| 1, …, 7 | control volumes, Fig. 2 | *Superscript* | |
| 12 | interaction between CV1 and CV2 | ° | standard conditions [gases at 1 atm, 25 °C, species in solution at 1 M, where M is the molarity = (moles solute)/(liters solution)] |
| 23 | interaction between CV2 and CV3 | | |
| 34 | interaction between CV3 and CV4 | | |
| 45 | interaction between CV4 and CV5 | ~ | dimensionless variable |

in potassium hydroxide, and more recently, the use of solid anionic membranes which are meant to eliminate the carbon dioxide problem [6], such as the ammonium-based Alkaline Anion-Exchange Membranes (AAEMs) [7]. In the flowing electrolyte type, a sufficiently open matrix is used to allow for liquid electrolyte circulation to reduce poisoning effects [8], and the old electrolyte may be exchanged for a fresh one, as the AFC becomes poisoned.

Considering static electrolyte cells, the use of asbestos or ammonium-based membranes for commercial applications also bring additional restrictions, based on ammonia potential hazardous effects, such as acute toxicity [9] and Immediately Dangerous to Life or Health (IDLH) levels [10], and on asbestos being a known carcinogenic agent [11]. Therefore, recently a cellulose-based alkaline membrane fuel cell was proposed [12]. A general view of the utilized experimental rig and of the cellulose-based membrane AMFC prototype is shown in Fig. 1a and b, respectively. Although promising experimental results were obtained in the laboratory, design and operating parameters need to be optimized for maximum performance, so that a proper assessment can be made for possible future commercialization. For that, mathematical modeling and computational simulation is recommended in order to predict how fuel cell performance is affected by the variation of operating and geometric parameters [13]. It is also important that the mathematical model accounts for temperature spatial gradients and gas channels pressure drops [13,14] which significantly affect fuel cell performance. Such desired model features should not lead to the understanding that the more complex the better the model will be. On the contrary, when the model is considered for fuel cell structure optimization, a large number of different configurations tests are needed, then it is desirable for the model to be simple, computationally fast and still able to capture reliably the fuel cell behavior [1,14].

Proton exchange membrane fuel cells (PEMFC) and solid oxide fuel cells (SOFCs) are considered the most promising candidates for commercial exploitation, and much attention has been given toward system modeling, including the fluid flows that supply the cells with fuel and oxidant, with the use of computational fluid dynamics (CFD), as pointed out by Young [15] and Ma et al. [16], that recently reviewed the status of three-dimensional fuel cell modeling. On the other hand, there are few previous studies concerning AFC modeling and simulation. For example, Vargas et al. [1] performed the AFC internal structure thermodynamic optimization introducing a dynamic mathematical model that accounted for temperature and pressure spatial gradients; Verhaert et al. [17] presented a steady state AFC thermodynamic model without the consideration of possible temperature variation within the cell using a control volume approach, which was validated by experimental data for future fuel cell stack development; Duerr et al. [18] used an isothermal dynamic electrochemical model to predict the effect of several parameters on an AFC stack response during load change events; Mohan and Shrestha [19] investigated the effect of four different electrolyte concentrations and three different anode flow rates on AFC performance experimentally and with an isothermal steady state model, concluding that performance increased as electrolyte concentration increased, and deduced statistically from modeling and statistical analysis optimal electrolyte concentration and anode flow rate for maximum performance, and Weydahl et al. [20] introduced an isothermal, one-dimensional transient model of a porous oxygen electrode in an alkaline medium based on mass balances and flooded-agglomerate theory in order to study time constants, the combined effects of fast potential propagation and slow oxygen diffusion targeting the dynamic improvement of the AFC cathodes without sacrifice of a steady state response. However, no studies were found in the open literature on transient mathematical models designed specifically for single alkaline membrane fuel cells (AMFC) that consider all of their internal components.

Though very useful refined information can be extracted from spatially dependent models, the two- and three-dimensional

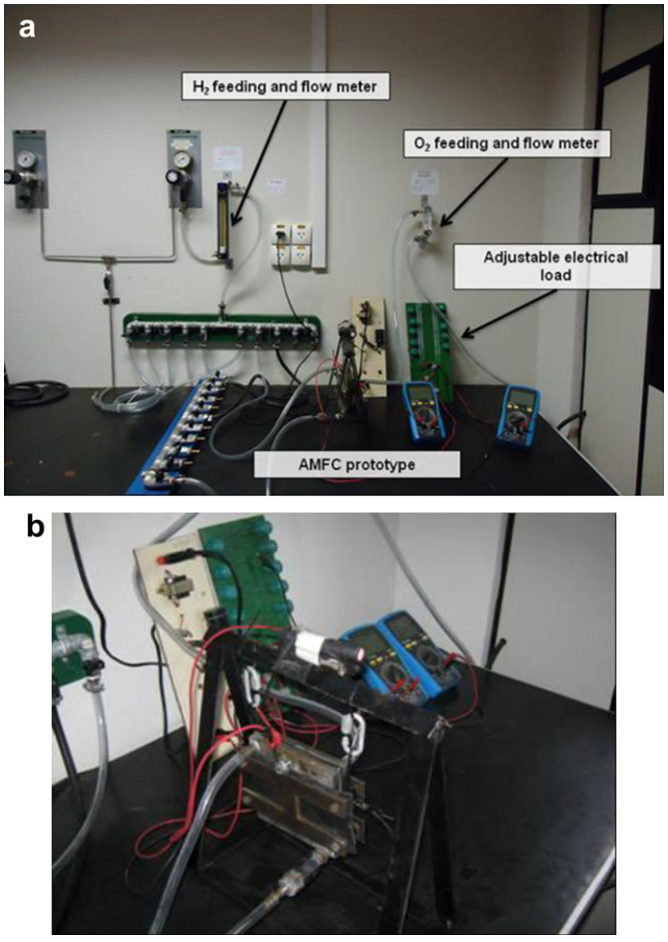


**Fig. 1.** (a) Fuel cell testing worktop; (b) Alkaline Membrane Fuel Cell prototype.

models are not suitable for the optimization of flow geometry, because they would require the solving of partial differential equations for flow simulation in a very large number of flow configurations. Therefore, in this paper a mathematical model is introduced for the single AMFC, which divides the fuel cell into several control volumes that correspond to the most representative parts of the flow system. All the flow phenomena that are present are taken into account. The result is a model with unidirectional internal flow that contains additional three-dimensional features such as the electrode wetted area, heat transfer between the cell, fuel, oxidant and the surroundings, and pressure drops in the gas channels. The model comprises a system of ordinary differential equations, the solution of which consists of the temperatures and pressures of each control volume, and the polarization and net power curves for the whole system. The model is simple enough to ensure small computational time requirements, so that it is possible to predict the response of the single AMFC according to variations of the material physical properties, and operating and design parameters.

The mathematical model is then experimentally validated using 5 (five) different sets of measured data obtained for the cellulose-based AMFC shown in Fig. 1 for several electrolyte concentrations. First, the inverse problem of parameters estimation methodology is used to elaborate an empirical correlation for the electrodes exchange current density as a function of electrolyte concentration using 3 (three) data sets, therefore adjusting the mathematical model. After that, the conditions corresponding to the other 2 (two) data sets are computationally simulated with the adjusted model to verify the agreement between numerical and experimental results, so that the model could be considered experimentally validated for simulation, control, design and optimization purposes.

## 2. Mathematical model

The mathematical model is based on an AFC model introduced previously [1], with the inclusion of pressure drop in the gas channels, heat generated by overpotential losses and the cellulose-based alkaline membrane. Although the single AFC mathematical model has been presented by the authors before [1], considerable modifications have been introduced in order to appropriately capture the AMFC behavior. Also, the nondimensionalization of the fuel cell geometry has been improved to account for a realistic fuel cell total fixed volume engineering design constraint, i.e., the finite space availability. Hence, in order to provide a clear understanding of the model and the experimental validation procedure, it is instructive to summarize its main features together with the new aspects.

The fuel cell is divided into seven control volumes (CV) that interact energetically with each other and with the environment as shown schematically in Fig. 2. The seven control volumes are: fuel channel (CV1), the anode diffusion layer (CV2), the anode reaction layer (CV3), the cellulose-based alkaline membrane (CV4), the cathode reaction layer (CV5), the cathode diffusion layer (CV6) and the oxidant channel (CV7).

The model consists of writing mass, energy and species conservation equations for each control volume, considering the chemical reactions on CV3 and CV5. All flow phenomena are considered, resulting on a time dependent unidirectional internal flow model. In the balance of energy, the heat generated by the electrochemical reactions and the potential losses are taken into account. The heat generation mechanism is due to ohmic resistance (throughout the fuel cell), as well as by activation and concentration overpotential losses in CV3 and CV5.

The solution of the differential and algebraic equations yields temperature and pressure profiles for each control volume, and polarization and power curves of the system as well. The actual electrical potential and power are obtained by subtracting from the reversible potential the losses due to surface overpotentials (poor electrocatalysis), slow diffusion and all internal ohmic losses through the cell (resistance of individual cell components, including electrolyte membrane, bipolar plates, interconnects and any other cell components through which electrons flow). These are functions of cell voltage or of the total cell current (I), which have a one-to-one relationship with each other. Since the external load determines the fuel cell operating current, in this treatment the total cell current is considered the independent variable. For the sake of generality, and for control and real time operation purposes, the following analysis is for unsteady state.

### 2.1. Fuel cell geometry

Fig. 2 shows all the external geometric parameters of the fuel cell. $L_x$ is the total length of the fuel cell (flow direction), $L_j$ the length of each control volume of the AMFC, such that $1 \leq j \geq 7$. $L_y$ and $L_z$ are the height and the thickness, respectively.

The total volume of the fuel cell, $V_T = L_x\, L_y\, L_z$, is finite and fixed. This is a realistic design constraint, which accounts for the finiteness of the available space and the general push for doing the most with limited resources (e.g., space), so that the maximization of performance for the specified volume means the maximization of performance *density*. The fixed length scale $V_T^{1/3}$ is used for the purpose of nondimensionalizing all the lengths that characterize the fuel cell geometry, as follows:

$$\xi_j = \frac{L_j}{V_T^{1/3}} \tag{1}$$

where the subscript j indicates a particular dimension of the fuel cell geometry, Fig. 2.

The wall heat transfer area of one control volume is $A_{wi} = p_s\, L_i$ $(2 \leq i \leq 6)$ and $A_{wi} \cong p_s\, L_i + L_y L_z$ $(i = 1, 7$; assuming that $L_t << L_c$ in Fig. 2), where $p_s = 2\,(L_y + L_z)$ is the perimeter of the fuel cell cross-section. The control volumes are $V_j = L_y\, L_z\, L_j$ $(2 \leq j \leq 6)$ and $V_j = n_c\, L_c\, L_j\, L_z$ $(j = 1, 7)$, where $n_c$ is the integer part of $L_y/(L_t + L_c)$, i.e., the number of parallel ducts in each gas channel (fuel and oxidant).

### 2.2. Dimensionless variables

Dimensionless variables are defined based on system geometry and operating parameters. Temperature and pressure are referenced to ambient conditions ($T_\infty$ and $p_\infty$), $\theta_i = T_i/T_\infty$ and $P_i = p_i/p_\infty$.

Dimensionless mass flow rate ($\psi$), global wall heat transfer coefficient ($N$), heat transfer coeficient ($\tilde{h}$), thermal conductivity ($\tilde{k}$), area ($\tilde{A}$), specific heat ($\gamma$), and time ($\tau$) are defined as follows:

$$\psi_i = \frac{\dot{m}_i}{\dot{m}_{ref}},\quad N_i = \frac{U_{wi} V_T^{2/3}}{\dot{m}_{ref} c_{p,f}},\quad \tilde{h}_i = \frac{h_i V_T^{2/3}}{\dot{m}_{ref} c_{p,f}},\quad \tilde{k}_i = \frac{k_i V_T^{1/3}}{\dot{m}_{ref} c_{p,f}},$$
$$\tilde{A}_i = \frac{A_i}{V_T^{2/3}},\quad \gamma_i = \frac{c_{p,i}}{c_{v,i}},\quad \tau = \frac{t}{t_{ref}} \tag{2}$$

where subscript i indicates a substance or a location in the fuel cell, $\dot{m}_{ref} = p_\infty V_T/(R_f T_\infty t_{ref})$ is a reference mass flow rate, and $R_f$ the ideal gas constant of the fuel, and $t_{ref}$ a specified reference time.

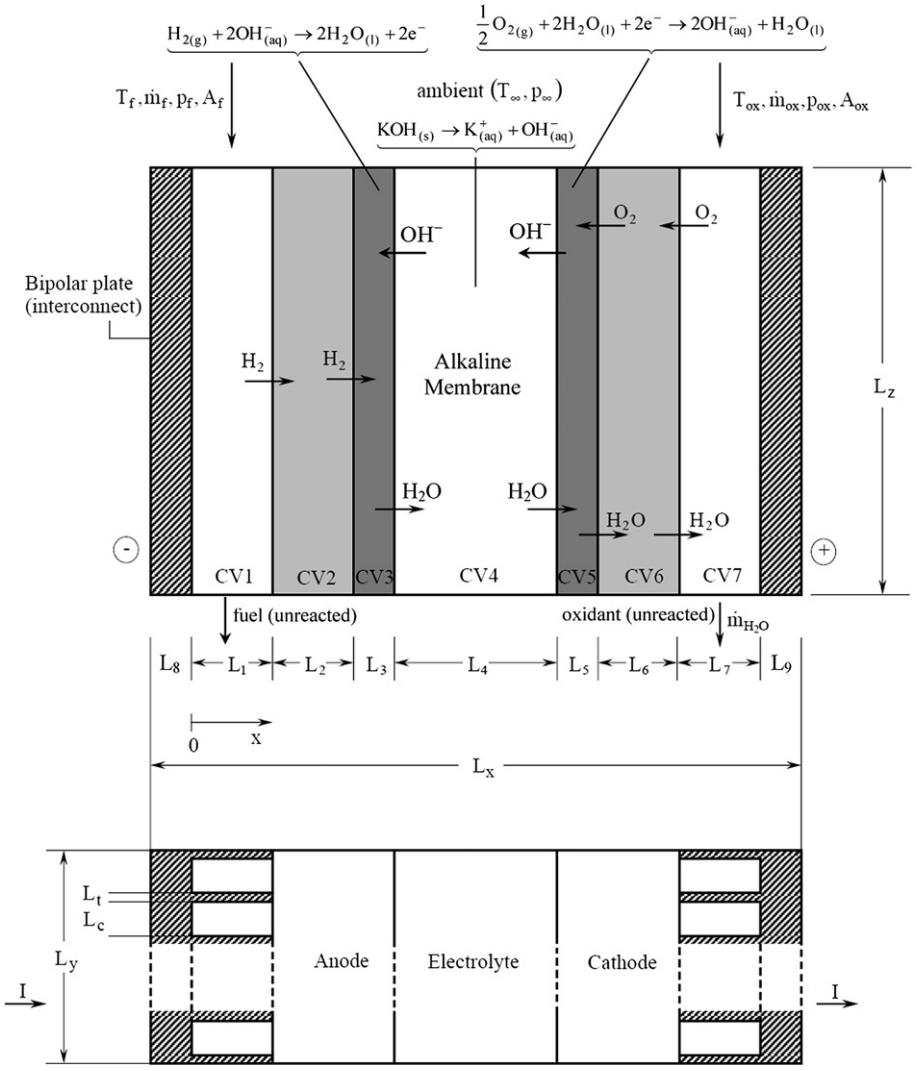


**Fig. 2.** The internal structure of a single AMFC.

### 2.3. Mass balance

The hydrogen mass flow rate required by a single AMFC for the current ($I$) dictated by the external load is

$$\dot{m}_{H_2} = \dot{n}_{H_2} M_{H_2} = \frac{I}{nF} M_{H_2} \tag{3}$$

Where $\dot{n}$ is the molar flow rate, kmol $s^{-1}$; $M$ the molar weight, kg $kmol^{-1}$; $n$ the equivalent electron per mole of reactant, eq $mol^{-1}$; $I$ the total current, A, and F the Faraday constant, C $eq^{-1}$. Accordingly, the oxygen mass flow rate needed for a single AMFC is $\dot{m}_{O_2} = 1/2\dot{n}_{H_2} M_{O_2}$. For simplicity of the analysis, it is hereby defined that $\dot{n}_{O_2} = 2\dot{m}_{O_2}/M_{O_2}$, so that $\dot{n}_{O_2} = \dot{n}_{H_2}$.

### 2.4. Energy conservation

#### 2.4.1. Fuel and Oxidant Channels (CV1 and CV7)

The fuel (hydrogen) enters the system through the CV1 channels and the oxidant (oxygen) through the CV7 channels, as shown in Fig. 2.

The mass and energy balances for CV1 state that:

$$\frac{d\theta_1}{d\tau} = \left[\tilde{Q}_{w1} + \psi_f\left(\theta_f - \theta_1\right) + \tilde{Q}_{12} + \tilde{Q}_{1ohm}\right] \frac{\theta_{1,0}\gamma_f}{P_f n_c \xi_1 \xi_c \xi_z} \tag{4}$$

where $\theta$ is the dimensionless temperature, $\tilde{Q}_i = \dot{Q}_i/\dot{m}_{ref} c_{p,f} T_\infty$ the dimensionless heat transfer rate, $\tilde{Q}_{12} = \tilde{h}_1 \tilde{A}_s (1-\varphi_2)(\theta_2 - \theta_1)$, $\tilde{Q}_{wi} = N_i \tilde{A}_{wi}(1-\theta_i)$, $\tilde{Q}_{iohm} = I^2 \beta_i/(\dot{m}_{ref} c_{p,f} T_\infty)$, $\beta$ the electrical resistance, $\theta_{i,0}$ the initial condition, $\phi$ the porosity, $\tilde{A}_s = L_y L_z / V_T^{2/3}$, $\psi_f = \zeta_1 \psi_{H_2}$, and $\zeta$ the stoichiometric ratio which is assumed greater than 1 on both sides.

The pressure drop in the channels is calculated using the ideal gas model and assuming that the channels are straight and sufficiently slender, as follows:

$$\Delta P_i = \left[f_i\left(\frac{\xi_z}{\xi_i} + \frac{\xi_z}{\xi_c}\right)\right] \frac{P_j}{\theta_i} \frac{R_f}{R_j} \tilde{u}_i^2 \tag{5}$$

where $i = 1, 7$ and $j = f$, ox, respectively. Here $\tilde{u}_i = (\tilde{u}_{i,in} + \tilde{u}_{i,out})/2$ is the gas dimensionless mean velocity in the channel, defined as $\tilde{u} = u/(R_f T_\infty)^{1/2}$, f is the friction factor. According to mass conservation, the flow dimensionless mean velocities in the gas channels are $\tilde{u}_1 = C\theta_1(\psi_f - \psi_{H_2}/2)/(\tilde{A}_{c1} P_f)$,

$\tilde{u}_7 = R_{ox}C\theta_7(\psi_{ox} - \psi_{O_2}/2)/(R_f\tilde{A}_{c7}P_{ox})$, where $C = (R_fT_\infty)^{1/2}\dot{m}_{ref}/(p_\infty V_T^{2/3})$, and $\tilde{A}_{ci} = n_cL_cL_i/V_T^{2/3}$, i = 1, 7, is the dimensionless total duct cross-section area in the fuel and oxidant channels, respectively.

The Reynolds number is monitored to determine flow regimes. Appropriate correlations are used according to the observed flow regime [21,22], as follows:

Laminar Regime - $Re_{Dh}$<2300 [21]

$$f_iRe_{D_{h,j}} = 24\left(1 - 1.3553\delta_i + 1.9467\delta_i^2 - 1.7012\delta_i^3 + 0.9564\delta_i^4 - 0.2537\delta_i^5\right) \quad (6)$$

$$\frac{h_iD_{h,i}}{k_i} = 7.541\left(1 - 2.610\delta_i + 4.970\delta_i^2 - 5.119\delta_i^3 + 2.702\delta_i^4 - 0.504\delta_i^5\right) \quad (7)$$

Turbulent Regime [22]

$$f_i = 0.079Re_{D_{h,i}}^{-1/4} \quad \left(2300 < Re_{D_{h,i}} < 5\times10^6\right) \quad (8)$$

$$\frac{h_iD_{h,i}}{k_i} = \frac{(f_i/2)(D_{h,i} - 10^3)Pr_i}{1 + 12.7(f_i/2)^{1/2}(Pr_i^{2/3} - 1)} \quad \left(2300 < Re_{D_{h,i}} < 5\times10^6\right) \quad (9)$$

where $\delta_i = L_c/L_i$, $D_{h,i} = 2L_cL_i/(L_t + L_c)$ for $i$ = 1,7, and $Re_{D_{h,i}} = u_iD_{h,i}\rho_i/\mu_i$.

The overall fuel cell reaction and the mass balance for CV7 yield $\dot{n}_{H_2O} = \dot{n}_{H_2O,out} = \dot{n}_{H_2O,in} = \dot{n}_{O_2}$. Therefore, the mass and energy balances for CV7 state that:

$$\frac{d\theta_7}{d\tau} = \left[\tilde{Q}_7 + \tilde{H}_{H_2O}(\theta_6) - \tilde{H}_{H_2O}(\theta_7) + \psi_{ox}\frac{c_{p,ox}}{c_{p,f}}\cdot(\theta_{ox} - \theta_7)\right] \times \frac{R_{ox}}{R_f}\frac{\gamma_{ox}\theta_{7,0}}{P_{ox}n_c\xi_c\xi_7\xi_z} \quad (10)$$

where $\tilde{Q}_7 = -\tilde{Q}_{67} + Q_{w7} + Q_{7ohm}$, $\tilde{Q}_{67} = \tilde{h}_7\tilde{A}_s(1-\varphi_6)(\theta_7 - \theta_6)$, and the dimensionless enthalpy of formation of a compound is defined as $\tilde{H}_i = \dot{n}_iH_i/(\dot{m}_{ref}c_{p,f}T_\infty)$ where the subscript i refers to a substance or a control volume.

*2.4.2. Anode and cathode diffusion layer (CV2 and CV6)*

The electrode is divided in two parts: diffusive layer and reactive layer. The purpose of the diffusion layer is to provide gas uniformly to the reactive layer and to remove the byproducts of the reaction. The diffusion layer is made hydrophobic to avoid the electrolyte solution to go to the gas stream. Therefore, it is considered that there is only hydrogen in the anode diffusion layer (CV2) and oxygen and water (product of the oxygen reduction reaction) in the cathode diffusion layer (CV6).

Diffusion is assumed to be the dominant mass transfer mechanism in the diffusion and catalytic layers. As the friction of the substances with the pore walls is considered, the Knudsen flow is used to represent the fuel and oxidant mass flow [23], as follows:

$$j_i = -[D(\rho_{out} - \rho_{in})/L]_i, \quad i = 2,6 \quad (11)$$

where $D = B\cdot[r\cdot(8\overline{R}T/\pi M)^{1/2}\cdot\varphi^q]$ is the Knudsen diffusion coefficient, r the pore radius, $\rho$ the density, $\overline{R}$ the universal gas constant, M the gas molecular weight, $\varphi$ the porosity, $q$ the tortuosity [1,24,25], and $B$ a dimensionless coefficient.

The output pressure of the diffusive layer, which is equal to the input pressure of the catalyst layer, is obtained using Eq. (11) and the ideal gas model, as follows:

$$P_{i,out} = P_{i,in} - \frac{j_iR_iT_\infty L_i\theta_i}{D_ip_\infty} \quad i = 2,6 \quad (12)$$

where $j_2 = \dot{m}_{H_2}/A_{3,wet}$ and $j_6 = \dot{m}_{O_2}/A_{5,wet}$, and $A_{3,wet}$ and $A_{5,wet}$ are the wetted areas in the porous catalyst layers. Note also that $P_{2,in} = P_f$ and $P_{6,in} = P_{ox}$. The average pressures in CV2 and CV6 are estimated as $P_i = 1/2(P_{i,in} + P_{i,out})$, i = 2, 6

The wetted areas in the porous catalyst layers $A_{3,wet}$ and $A_{5,wet}$ are estimated by considering dual-porosity sintered metal electrodes, in which the average pore diameter is considered to be roughly the same order as the square root of the porous medium permeability [1]. In this consideration the pores are approximated as parallel tubes, i.e., $A_{j,wet} = \{4\varphi_jL_jK_j^{-1/2} + (1-\varphi_j)\}A_s$.

Hydrogen diffuses through CV1 and CV3 and oxygen and water vapor diffuse through CV5, CV6 and CV7. Therefore, the mass and energy balances for CV2 state that

$$\frac{d\theta_2}{d\tau} = \left[(\theta_1 - \theta_2) + \frac{\tilde{Q}_2}{\psi_{H_2}}\right]\frac{\gamma_{s,a}\psi_{H_2}}{\rho_{s,a}(1-\phi_2)\xi_2\xi_y\xi_z} \quad (13)$$

where $\tilde{Q}_2 = -\tilde{Q}_{12} + \tilde{Q}_{W2} + \tilde{Q}_{23} + \tilde{Q}_{2ohm}$, $\tilde{Q}_{23} = \tilde{k}_{s,a}(1-\varphi_2)\tilde{A}_s(\theta_2 - \theta_3)/[(\xi_2 + \xi_3)/2]$, $\tilde{\rho}_i = \rho_iR_fT_\infty/p_\infty$, $\gamma_{s,a} = c_{p,f}/c_{v,s,a}$, and the subscript s,a and s,c mean the solid part of the anode and cathode, respectively.

The mass balance for CV6, yields $\dot{m}_{O_{2,out}} = \dot{m}_{O_{2,in}} = \dot{m}_{O_2}$ and $\dot{n}_{H_2O} = \dot{n}_{H_2O,out} = \dot{n}_{H_2O,in} = \dot{n}_{O_2}$. The mass and energy balances for CV6 state that

$$\frac{d\theta_6}{d\tau} = \left[\tilde{Q}_6 + \psi_{O_2}\frac{c_{p,ox}}{c_{p,f}}(\theta_7 - \theta_6) + \tilde{H}(\theta_5)_{H_2O} - \tilde{H}(\theta_6)_{H_2O}\right] \times \frac{\gamma_{s,c}}{\tilde{\rho}_{s,c}(1-\varphi_6)\xi_6\xi_y\xi_z} \quad (14)$$

where $\tilde{Q}_6 = -\tilde{Q}_{56} + \tilde{Q}_{W6} + \tilde{Q}_{67} + \tilde{Q}_{6ohm}$, $\tilde{Q}_{56} = \tilde{k}_{s,c}(1-\varphi_6)\tilde{A}_s(\theta_5 - \theta_6)/[(\xi_5 + \xi_6)/2]$, and $\gamma_{s,c} = c_{p,f}/c_{v,s,c}$.

*2.4.3. Anode and cathode reaction layer (CV3 and CV5)*

The anode (CV3) is assumed to contain the porous electrode, fuel (hydrogen) and electrolyte aqueous solution (KOH) that is present in the pores of the electrode. The electrons released by the oxidation of the hydrogen in CV3 pass through an external circuit and participate in the reduction of the oxygen in CV5. The cathode (CV5) is assumed to contain the porous electrode, oxygen and the electrolyte.

The Hydrogen Oxidation Reaction (HOR) and the Oxygen Reduction Reaction (ORR) are written as follows

$$H_{2(g)} + 2OH^-_{(aq)} \rightarrow 2H_2O_{(l)} + 2e^- \quad (15)$$

$$\frac{1}{2}O_{2(g)} + 2H_2O_{(1)} + 2e^- \rightarrow 2OH^-_{(aq)} + H_2O_{(1)} \quad (16)$$

In CV3 and CV5, the mass of liquid contained in these CVs is assumed to be negligible compared to the solid mass of the electrode for the thermal analysis. CV3 and CV5 interact thermally with the adjacent control volumes by conduction and the with the ambient by convection. Heat is generated by the electrochemical reactions and by the irreversible mechanisms (ohmic resistance, activation and concentration overpotential losses).

Among the model enhancements of the present study are the inclusions of the heat generation due to activation overpotential losses ($\eta_a$) and concentration overpotential losses ($\eta_{d,a}$). However, the ohmic heat generated in CV3, CV4 and CV5, due to the ion transport resistance of the solution and the electric resistance of their solid components has been previously considered for the AFC model [1]. The calculations of overpotential losses ($\eta_a$, $\eta_{d,a}$ and $\eta_{ohm}$) are presented in the electrochemical model section of this study.

The mass and energy balances for CV3, together with the anode reaction equation, deliver the relations $\dot{n}_{H_2} = \dot{m}_f/M_{H_2}$, $\dot{n}_{H_2O} = 2\dot{n}_{H_2}$, $\dot{m}_{H_2O} = 2\dot{n}_{H_2}M_{H_2O}$, $\dot{n}_{OH^-} = 2\dot{n}_{H_2}$, $\dot{m}_{OH^-} = 2\dot{n}_{H_2}M_{OH^-}$ and

$$\frac{d\theta_3}{d\tau} = \left[\tilde{Q}_3 - \Delta\tilde{H}_3 + \Delta\tilde{G}_3\right] \frac{\gamma_{s,a}}{\tilde{\rho}_{s,a}(1-\phi_3)\xi_3\xi_y\xi_z} \tag{17}$$

where $\tilde{Q}_{3,act} = \eta_a I/(m_{ref}c_{p,f}T_\infty)$, $\tilde{Q}_{3,dif} = \eta_{d,a}I/(\dot{m}_{ref}c_{p,f}T_\infty)$, $\tilde{Q}_3 = -\tilde{Q}_{23} + \tilde{Q}_{w3} + \tilde{Q}_{34} + \tilde{Q}_{3ohm} + \tilde{Q}_{3,act} + \tilde{Q}_{3,dif}$, and $\tilde{Q}_{34} = -(1-\varphi_3)(\theta_3-\theta_4)2\tilde{A}_s k_{s,a}k_{memb}/(\xi_4\tilde{k}_{s,a} + \xi_3\tilde{k}_{memb})$.

Analogously, the mass and energy balances in CV5, and the cathode reaction equation deliver $\dot{n}_{H_2O,in} = 2\dot{n}_{H_2O,out} = \dot{n}_{O_2}, \dot{n}_{OH^-_{out}} = 2\dot{n}_{O_2}$, and

$$\frac{d\theta_5}{d\tau} = \left[\tilde{Q}_5 - \Delta\tilde{H}_5 + \Delta\tilde{G}_5\right] \frac{\gamma_{s,c}}{\tilde{\rho}_{s,c}(1-\varphi_5)\xi_5\xi_y\xi_z} \tag{18}$$

where $\tilde{Q}_{5,act} = \eta_c I/(m_{ref}c_{p,f}T_\infty)$, $\tilde{Q}_{5,dif} = \eta_{d,c}I/(m_{ref}c_{p,f}T_\infty)$, $\tilde{Q}_5 = -\tilde{Q}_{45} + \tilde{Q}_{w5} + \tilde{Q}_{56} + \tilde{Q}_{5ohm} + \tilde{Q}_{5,act} + \tilde{Q}_{5,dif}$, and $\tilde{Q}_{45} = -(1-\varphi_5)(\theta_4-\theta_5)2\tilde{A}_s k_{s,c}k_{memb}/(\xi_4\tilde{k}_{s,c} + \xi_5\tilde{k}_{memb})$.

Eqs. (17) and (18) account for the reactions dimensionless enthalpy and free Gibbs energy variations $(\Delta\tilde{H}_3, \Delta\tilde{G}_3) = \dot{n}_{H_2}(\Delta H_3, \Delta G_3)/(\dot{m}_{ref}c_{p,f}T_\infty)$ and $(\Delta\tilde{H}_5, \Delta\tilde{G}_5) = \dot{n}_{H_2}(\Delta H_5, \Delta G_5)/(\dot{m}_{ref}c_{p,f}T_\infty)$.

The molar enthalpies of formation are obtained from tabulated values [26,27,28] at 1 atm, since $\Delta H$ is independent of pressure, and in the following temperatures: $T_2$ for $H_{2(g)}$, $T_4$ for $OH^-_{(aq)}$ and $T_3$ for $H_2O_{(l)}$. For CV5, values are used also at 1 atm and at $T_6$ for $O_{2(g)}$, $T_4$ for the reactant $H_2O_{(l)}$, $T_5$ for the product $H_2O_{(l)}$ and $OH^-_{(aq)}$.

The molar enthalpy change due to the anode reaction is given by $\Delta H_3 = \sum_{products}[\nu_i H_i(T_i)] - \sum_{reactants}[\nu_i H_i(T_i)]$ and $W_{e3} = -\Delta G_3$, $\Delta H_3$ is the CV3 reaction enthalpy change (kJ kmol$^{-1}H_2$); $\nu_i$ are the stoichiometric coefficients; $H_i(T_i)$ is the molar enthalpy (kJ kmol$^{-1}$) of formation at a temperature $T_i$ of reactants and products of compound i; $\Delta G_3$ is the CV3 reaction Gibbs free energy change (kJ kmol$^{-1}H_2$), and $W_{e3}$ is the maximum (reversible) electrical work generated due to the reaction in CV3 (kJ kmol$^{-1}H_2$).

The reaction Gibbs free energy change $\Delta G$ is a function of temperature, pressure and concentrations,

$$\Delta G = \Delta G^\circ + \overline{R}T\ln Q \tag{19}$$

where $\Delta G^\circ = \Delta H^\circ - T\Delta S^\circ$ is the standard Gibbs free energy (kJ kmol$^{-1}H_2$); $\Delta H^\circ$ is the standard enthalpy change (kJ kmol$^{-1}$); $\Delta S^\circ$ is the standard entropy change (kJ kmol$^{-1}$ K) [gases at 1 atm, 25 °C, species in solution at 1 M, where M is the molarity = (moles solute)/(liters solution)], and Q is the reaction quotient. In the present reaction [Eq. (15)] the resulting expression for $Q_3$ is $Q_3 = \{[OH^-_{(aq)}]^2 p_{H_2}\}^{-1}$, where $[OH^-_{(aq)}]$ is the molar concentration of the alkaline solution and $p_{H2} = p_{2,out}$, i.e., the $H_2$ partial pressure at the CV2 outlet.

The dissolution of potassium hydroxide in water is represented by the following chemical equation:

$$KOH_{(S)} \rightarrow K^+_{(aq)} + OH^-_{(aq)} \tag{20}$$

The molar concentration of KOH, [KOH], is obtained from the weight percentage of KOH in solution, $y$.

For the cathode (CV5), $\Delta H$ and $\Delta G$ are obtained similarly to the CV3 analysis, obtaining $\Delta H_5$ and $W_{e5} = -\Delta G_5$. The CV5 reaction quotient is $Q_5 = [OH^-]^2/p_{O_2}^{1/2}$, in which $p_{O2} = p_{6,out}$.

### 2.4.4. Electrolyte and membrane (CV4)

Typical AFC electrolytes are aqueous solutions of KOH. In the AMFC, the electrolyte comprises an aqueous solution of KOH supported by an inert solid medium. In the prototype shown in Fig. 1, a cellulose-based membrane is utilized.

Eqs. (15) and (16) and the conservation of mass in CV4 require that $2\dot{n}_{H_2} = \dot{n}_{OH^-,out} = \dot{n}_{OH^-,in} = 2\dot{n}_{O_2}$, $2\dot{n}_{H_2} = \dot{n}_{H_2O,in} = \dot{n}_{H_2O,out} = 2\dot{n}_{O_2}$. In CV4 the mass of fluid is not negligible in presence of the cellulose-based membrane mass in the thermal analysis. Therefore, the mass and energy balances for CV4 state that

$$\frac{d\theta_4}{d\tau} = \left[\tilde{Q}_4 + \tilde{H}_{OH^-}(\theta_5) - \tilde{H}_{OH^-}(\theta_4) + \tilde{H}_{H_2O}(\theta_3) - \tilde{H}_{H_2O}(\theta_4)\right] \times \frac{\gamma_{memb}}{\tilde{\rho}_{memb}\xi_4\xi_y\xi_z} \tag{21}$$

where $\tilde{Q}_4 = -\tilde{Q}_{34} + \tilde{Q}_{w4} + \tilde{Q}_{45} + \tilde{Q}_{4ohm}$, $\rho_{memb} = \rho_{sol}\varphi_4 + \rho_{cel}(1-\varphi_4)$, $c_{p,memb} = c_{p,sol}\varphi_4 + c_{p,cel}(1-\varphi_4)$, and $k_{memb} = k_{sol}\varphi_4 + k_{cel}(1-\varphi_4)$.

## 2.5. Electrochemical model

Based on the electrical conductivities and geometry of each compartment, the electrical and ionic resistances, $\beta(\Omega)$, are given by:

$$\beta_i = \frac{\xi_i}{\tilde{A}_s V_T^{1/3}\sigma_i(1-\phi_i)}, \quad i = 1,2,6,7(\varphi_1,\varphi_7 = 0) \tag{22}$$

$$\beta_i = \frac{\xi_i}{\tilde{A}_s V_T^{1/3}\sigma_i\phi_i}, \quad i = 3,4 \text{ and } 5 \tag{23}$$

For i = 3, 4, and 5, $\sigma_i = \sigma_{sol}$. The conductivities of the diffusive layers, $\sigma_2$ and $\sigma_6$, are the carbon-phase conductivities [29]. Finally, the conductivities of CV1 and CV7, $\sigma_1$ and $\sigma_7$, are given by the electrical conductivity of the bipolar plate material.

The dimensionless potential and the dimensionless overpotential are defined in terms of a given reference voltage, $V_{ref}$, so that $\tilde{V}_i = V_i/V_{ref}$ and $\tilde{\eta}_i = \eta_i/V_{ref}$.

The actual potential ($\tilde{V}_i$) provided by a fuel cell results from the combination of anode irreversible potential ($\tilde{V}_{i,a}$), cathode irreversible potential ($\tilde{V}_{i,c}$) and the ohmic loss ($\tilde{\eta}_{ohm}$) that occurs throughout the fuel cell between CV1 and CV7, as follows:

$$\tilde{V}_i = \tilde{V}_{i,a} + \tilde{V}_{i,c} - \tilde{\eta}_{ohm} \tag{24}$$

$$\tilde{\eta}_{ohm} = \frac{I}{V_{ref}}\sum_{i=1}^{7}\beta_i \tag{25}$$

The reversible electrical potential at the anode and cathode are respectively given by the Nernst equation, as follows:

$$V_{e,j} = V^\circ_{e,j} - \frac{\overline{R}T_i}{nF}\ln Q_i \quad (i = 3,5 \text{ and } j = a,c, \text{ respectively}) \tag{26}$$

where $V_{e,j} = \Delta G_i/(-nF)$, $V^\circ_{e,j} = \Delta G^\circ_i/(-nF)$.

At the anode there are two mechanisms for potential losses: (i) charge transfer, and (ii) mass diffusion. The potential losses at the anode ($\eta_a$) and cathode ($\eta_c$) due to charge transfer are obtained implicitly from the Butler-Volmer equation for a given current $I$ [1,30,31], as follows:

$$\frac{I}{A_{i,\mathrm{wet}}} = i_{0,j}\left[e^{\frac{(1-\alpha_j)\eta_j F}{\overline{\mathrm{R}}\mathrm{T}_i}} - e^{-\frac{\alpha_j \eta_j F}{\overline{\mathrm{R}}\mathrm{T}_i}}\right] \quad (i = 3,5 \text{ and } j = \mathrm{a,c, \ respectively}) \tag{27}$$

where $\alpha_j$ are the anode and cathode charge transfer coefficients, and $i_{0,j}$ the anode and cathode exchange current densities, respectively.

The potential losses due to mass diffusion is [1,30]:

$$\eta_{\mathrm{d},j} = \frac{\overline{\mathrm{R}}\mathrm{T}_i}{\mathrm{nF}}\ln\left(1 - \frac{I}{A_{i,\mathrm{wet}} i_{\mathrm{Lim},j}}\right) \quad (i = 3,5 \text{ and } j = a,c, \text{ respectively}) \tag{28}$$

The limiting current densities in the anode and cathode ($i_{\mathrm{Lim},j}$) represent borderline cases for mass transfer, when the concentration of reactants in the catalyst layer located at the interface with the gas diffusion layer drop to zero ($P_{2,\mathrm{out}} = 0$ and $P_{6,\mathrm{out}} = 0$). These are the maximum currents that a fuel cell can provide. For higher current values the system collapses. Then, Eq. (12) is re-written as follows:

$$i_{\mathrm{Lim},j} = \frac{P_{\mathrm{f}} p_\infty D_i \mathrm{nF}}{M_{\mathrm{H_2}} L_i R_{\mathrm{f}} T_\infty \theta_i} \quad (i = 2,6 \ \textit{and} \ j = a,c, \ \text{respectively}) \tag{29}$$

The resulting electrical potential at the anode and cathode are respectively given by

$$\tilde{V}_{i,j} = \tilde{V}_{\mathrm{e},j} - \tilde{\eta}_j - \left|\tilde{\eta}_{\mathrm{d},j}\right| \quad (j = a,c) \tag{30}$$

The absolute values of $\tilde{\eta}_{\mathrm{d},j}$ are used, because there could be $\tilde{\eta}_{\mathrm{d},j} < 0$ (cathodic overpotential).

### 2.6. Fuel cell net power output

In order to estimate the available power provided by a fuel cell ($\tilde{W}_{\mathrm{net}}$), it is necessary to subtract the energy needed to supply the fuel cell with fuel and oxidant ($\tilde{W}_{\mathrm{p}}$). Therefore the total net power (available for utilization) of the fuel cell is

$$\tilde{W}_{\mathrm{net}} = \tilde{W} - \tilde{W}_{\mathrm{p}} \tag{31}$$

where $\tilde{W} = \tilde{V}_i \tilde{I}$ is the total fuel cell electrical power output. The dimensionless pumping power, $\tilde{W}_{\mathrm{p}}$, is given by

$$\tilde{W}_{\mathrm{p}} = \psi_{\mathrm{f}} S_{\mathrm{f}} \frac{\theta_i}{P_i}\Delta P_1 + \psi_{\mathrm{ox}} S_{\mathrm{ox}} \frac{\theta_7}{P_7}\Delta P_7 \tag{32}$$

where $S_i = m_{\mathrm{ref}} T_\infty R_i / V_{\mathrm{ref}} I_{\mathrm{ref}}, \ i = f, ox.$

## 3. Numerical method

Eqs. (4), (10), (13), (14), (17), (18), (21), for dimensionless temperatures and Eq. (12) for dimensionless pressures, and the specified initial conditions form a system of 7 ordinary differential equations and 2 algebraic equations. The unknowns are $\theta_i$ and $P_i$, i.e., the temperatures in the seven control volumes, and the gas pressures at CV2 and CV6 outlets. Once the temperatures and pressures are known, the electrical potentials, and single AMFC electrical and net power are calculated for any current level.

Two numerical methods were used. The first method calculates the transient behavior of the system, starting from a set of initial conditions, then the solution is marched in time (and checked for accuracy) until a steady state is achieved at any current level. The equations are integrated in time explicitly using an adaptive time step, 4th-5th order Runge-Kutta method [32]. The time step is adjusted automatically according to the local truncation error, which is kept below a specified tolerance of $10^{-6}$. The second method is for the steady state solution. The time derivatives are dropped from Eqs. (4), (10), (13), (14), (17), (18), and (21),. Pressures are related to temperatures via Eq. (12). The system reduces to seven nonlinear algebraic equations, in which the unknowns are the temperatures of the seven control volumes. This system is solved using a quasi-Newton method [32]. Convergence was achieved when the Euclidean norm of the residual of the system was less than $10^{-6}$.

## 4. Experiments

### 4.1. Experimental set up

A purpose-built test facility was implemented in the laboratory for conducting fuel cell experiments, as shown in Fig. 1a. It consists of a worktop with $H_2$ and $O_2$ feeding systems with respective manometers and flowmeters mounted on the wall, an adjustable low power electric load, built with nickel-chrome alloy wire, and a supporting structure for single fuel cell testing.

A prototype of a new single AMFC, which includes a cellulose-based membrane impregnated with a solution of water and potassium hydroxide (KOH), was also built-in the laboratory, as shown in Fig. 1b. The membrane is composed of filter paper with a specially designed composition for proper electrolyte absorption and durability [12], providing a novel and inexpensive method of introducing the potassium hydroxide electrolyte into the cell. As shown in the exploded view of Fig. 3, in the design of the bipolar plates, a parallel channel configuration was utilized, so that proper uniform fuel and oxidant gas diffusion is achieved starting from the backing layer of the electrodes. The membrane is sandwiched between the two electrode sheets (anode and cathode). The solid electrolyte or the cellulose-based membrane is what differentiates this AMFC from other AMFC types. Feedback controlled humidifiers containing aqueous potassium hydroxide solution ensured that the membrane was not dried out by the flow and kept the mass fraction of KOH in the electrolyte at a constant value for continuous operation.

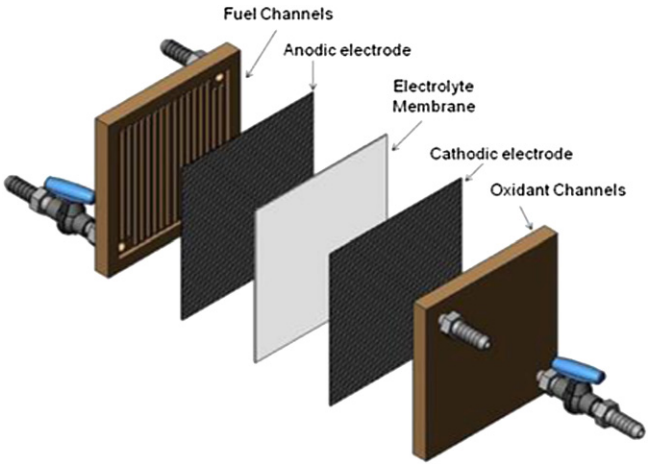


**Fig. 3.** Exploded view of the components of the single AMFC prototype.

The AMFC works with electrodes composed of nickel and cobalt that are electrodeposited onto each of the permeable carbon film sheets, that are made hydrophilic on the reactive side that face the electrolyte and hydrophobic on the side facing the gas channels. However, in order to perform the experimental validation of the mathematical model for this study as a base case, platinum-carbon electrode sheets were used, type LT-250-EW, from BASF, with the load of 5 g $m^{-2}$ of 30 wt. % Pt supported in Vulcan XC-72.

### 4.2. Experimental procedure

The experimental set up described in the previous section was used to gather the experimental data set required for the experimental validation of the mathematical model introduced in this study. Each test consisted of measuring the values of current and voltage in order to quantitatively describe the performance of the AMFC by polarization and power curves. This was done by varying the load resistance shown in Fig. 1a from open circuit (I = 0) to short circuit (maximum I) conditions.

The experimental work involved the acquisition of the AMFC prototype voltage and current output data in real time. This task was performed through the utilization of a computational data acquisition system which consisted of a digital multimeter board, NI PCI-4060, a NI PCI-6703 analog output board, and a SCXI-1127 32-channel high voltage multiplexer, all manufactured by National Instruments, USA, which allowed for the sequential data acquisition from 32 channels at interval times of 0.1 s. All the data were processed by a suitable software application to convert the signals into voltage, current and power readings.

Measurements of current and voltage were taken at three different times of the experiment: 0, 15 and 30 minutes. Using the adjustable load, and varying the load resistance progressively so that the entire cell current operating range was covered ($0 \le \tilde{I} \le \tilde{I}_{max}$), it was possible to obtain polarization and power curves for the AMFC prototype in the three time settings. Therefore three runs were considered for each membrane KOH concentration corresponding to the three time settings. Additionally, the whole experimental set up shown in Fig. 1 was inside a temperature controlled room, in which the air temperature was set to 25 °C. Steady state conditions were reached after 30 min before starting all the experiments. The voltage and current precision limits for each experiment were computed as two times the standard deviation of the 3 runs [33], so that it is assumed that the system response follows a symmetric unimodal normal distribution. Therefore, it is admissible to state that 95 % of the system responses exhibit actual voltage and current equal to the calculated mean (from the sample measurements) plus or minus twice the experimental measurements standard deviation [34]. Both the voltage and current bias limits were negligible in presence of the respective precision limits. Due to the low current range observed in the AMFC prototype ($0 \le \tilde{I} \le \tilde{I}_{max}$), pumping power was negligible in presence of electrical power, therefore $\tilde{W}_{net} \cong \tilde{W} = \tilde{V}\tilde{I}$. As a result, the measurements uncertainties to produce the error bars in the graphical results were calculated by:

$$\frac{U_{\tilde{V}}}{\tilde{V}} = \left[\left(\frac{P_{\tilde{V}}}{\tilde{V}}\right)^2 + \left(\frac{B_{\tilde{V}}}{\tilde{V}}\right)^2\right]^{1/2} \equiv \frac{P_{\tilde{V}}}{\tilde{V}} \quad \text{and} \qquad \frac{U_{\tilde{I}}}{\tilde{I}} = \left[\left(\frac{P_{\tilde{I}}}{\tilde{I}}\right)^2 + \left(\frac{B_{\tilde{I}}}{\tilde{I}}\right)^2\right]^{1/2} \cong \frac{P_{\tilde{I}}}{\tilde{I}} \tag{33}$$

$$\frac{U_{\tilde{W}_{net}}}{\tilde{W}_{net}} \cong \frac{U_{\tilde{W}}}{\tilde{W}} = \left[\left(\frac{U_{\tilde{V}}}{\tilde{V}}\right)^2 + \left(\frac{U_{\tilde{I}}}{\tilde{I}}\right)^2\right]^{1/2} \tag{34}$$

## 5. Results and discussion

In this section, the AMFC prototype behavior is studied experimentally and numerically. First, the cellulose-based membrane electrolyte solution KOH concentration effect on AMFC performance is analyzed. Then, the experimental measurements are used to experimentally validate the numerical results obtained with the mathematical model introduced in section 2, using 5 (five) different sets of measured data obtained for the cellulose-based AMFC shown in Fig. 1 for several electrolyte concentrations. The procedure consists of solving the inverse problem of parameters estimation to elaborate an empirical correlation for the electrodes exchange current density as a function of electrolyte concentration using 3 (three) data sets, therefore adjusting the mathematical model. After that, the conditions corresponding to the other 2 (two) data sets are computationally simulated with the adjusted model to verify the agreement between numerical and experimental results. Finally, the experimentally validated model is used to investigate the AMFC prototype response, temperature distribution and pressure drops.

### 5.1. The effect of KOH concentration on performance

The AMFC prototype of Fig. 1 has a fuel cell square section, i.e., $\xi_y/\xi_x = \xi_z/\xi_x = 3.95$, according to Fig. 2. The internal configuration is given by: $\xi_1/\xi_x = \xi_7/\xi_x = 0.0789$, $\xi_2/\xi_x = \xi_6/\xi_x = 0.0108$, $\xi_3/\xi_x = \xi_5/\xi_x = 0.0058$, $\xi_4/\xi_x = 0.0197$, $\xi_8/\xi_x = \xi_9/\xi_x = 0.3946$, $\xi_t/\xi_y = 0.02$, and $\xi_c/\xi_y = 0.01$. The bipolar plates (interconnects) comprise two parts: the gas channels (CV1 and CV7) and back plates that also act as mechanical support, which are represented by $L_8$ and $L_9$ in Fig. 2.

The AMFC response operating with six different conditions, varying the KOH mass fraction in the electrolyte solution (10 wt. % , 20 wt. % , 30 wt. % , 40 wt. % and 50 wt. % ), is shown in Fig. 4. The measurements of current and voltage were taken at three different times of the experiment: 0, 15 and 30 minutes. Since the AMFC prototype performance did not vary significantly on these three times for each experiment, it is reasonable to assume that the prototype startup transient is very short, which is probably due to the relatively small size of the cell, thus with low thermal inertia.

All experimental results for $t = 0$ min were grouped on Fig. 5 and summarized in Table 1, so that the voltage losses that occurred and the maximum current and power obtained in each test can be compared. The maximum power was obtained for $y_{opt} = 40$ wt. % , which shows that even without presenting the highest initial potential, the cell reached the highest short circuit current among all tested electrolyte solution mass fractions, and showed smaller potential losses than with the other concentrations, which produced the highest power among the tested KOH mass fractions. From the physical point of view, such optimum KOH mass fraction value is expected based on the analysis of two extremes, i.e., when $y \to 0$ %, hydroxyl ions become unavailable in the membrane, therefore $\dot{W} \to 0$, and when $y \to 100$%, the flow of ions decreases due to the reduction of liquid water in the control volume, and $\dot{W} \to 0$ as well. Therefore, there must exist an intermediate optimal value $y_{opt}$, so that $\dot{W}$ is maximized.

Fig. 6 summarizes the optimization results found through the experimental measurements. The experimental voltage and power measurements corresponding to different current levels are plotted in dimensionless form with error bars calculated according to Eqs. (33) and (34). Both maximum voltage and power were found for the AMFC prototype operating with y between 30 and 40 wt. % for three current levels ($\tilde{I} = 0.56$, 1.05, and 2.52). However, as current increases, maximum power is obtained when $y \to 40$ wt.%. In fact, with $y = 40$ wt.%, the AMFC reached the maximum power

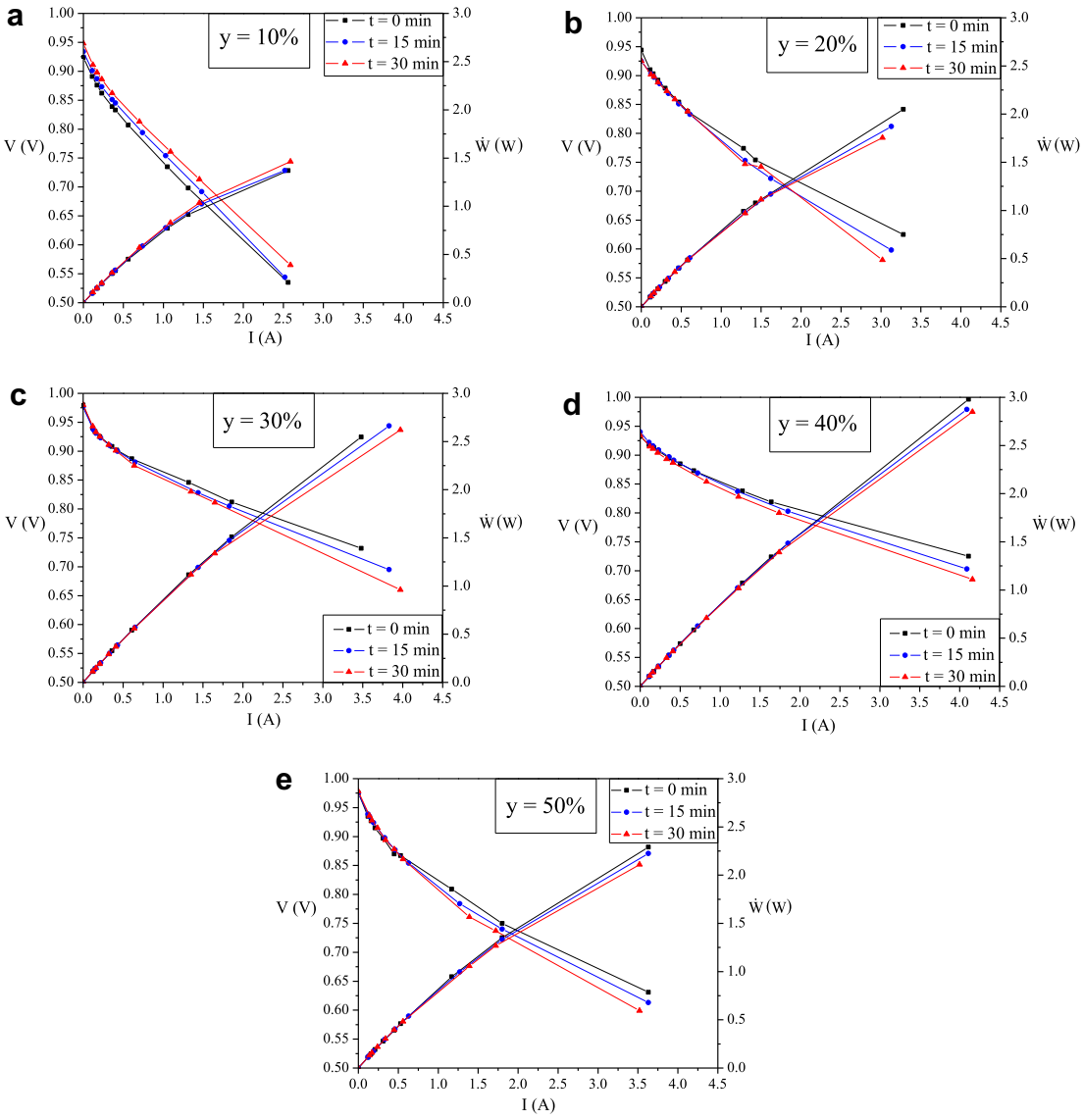


**Fig. 4.** AMFC prototype experimental potential and power responses for five different electrolyte solution mass fractions: y = 10 wt. % (a), 20 wt. % (b), 30 wt. % (c), 40 wt. % (d) and 50 wt. % (e).

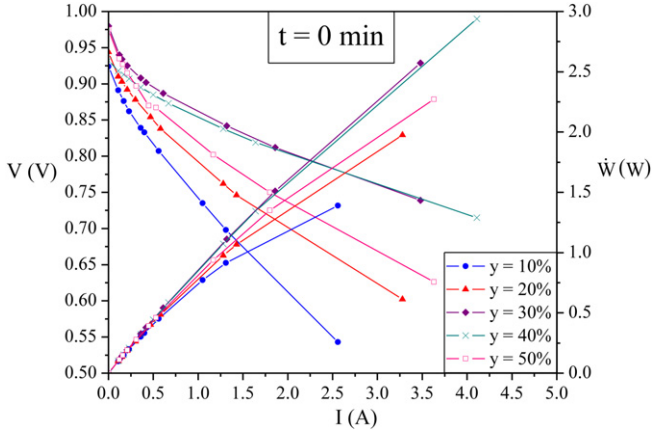


**Fig. 5.** Polarization and power curves experimentally obtained with different electrolyte mass fraction (y) values at t = 0 min.

and operating current in short circuit among all tested cases, indicating that the maximum performance is obtained for $y_{opt} = 40$ wt.% according to the experimental measurements.

The effect of KOH concentration on alkaline fuel cells has been investigated theoretically before by Zhang et al. [35] that conducted a multi-objective optimization of a typical alkaline fuel cell using

**Table 1**
Experimental values for open circuit and short circuit at $t = 0$ min.

| $y$ (wt. % KOH) | $i$ (A) | $V$ (V) | $\dot{W}$ (W) |
|---|---|---|---|
| 10 | 0.00 | 0.92 | 0.00 |
| | 2.56 | 0.54 | 1.39 |
| 20 | 0.00 | 0.94 | 0.00 |
| | 3.28 | 0.62 | 2.05 |
| 30 | 0.00 | 0.98 | 0.00 |
| | 3.48 | 0.73 | 2.55 |
| 40 | 0.00 | 0.93 | 0.00 |
| | 4.11 | 0.72 | 2.98 |
| 50 | 0.00 | 0.98 | 0.00 |
| | 3.63 | 0.63 | 2.29 |

a steady state alkaline fuel cell model. The authors reported an algebraic correlation to obtain the optimal KOH molar concentration for maximum alkaline fuel cell performance as a function of operating temperature. The present study corroborates experimentally the theoretically expected trend, although for a different alkaline fuel cell type, i.e., the herein proposed cellulose-based membrane alkaline fuel cell. Therefore, the optimal KOH concentration for maximum power output is a fundamental feature that should be pursued in any alkaline fuel cell type.

### 5.2. Experimental model adjustment and validation

A computational code was written in Fortran language based on the numerical method described in section 3 to obtain the solution

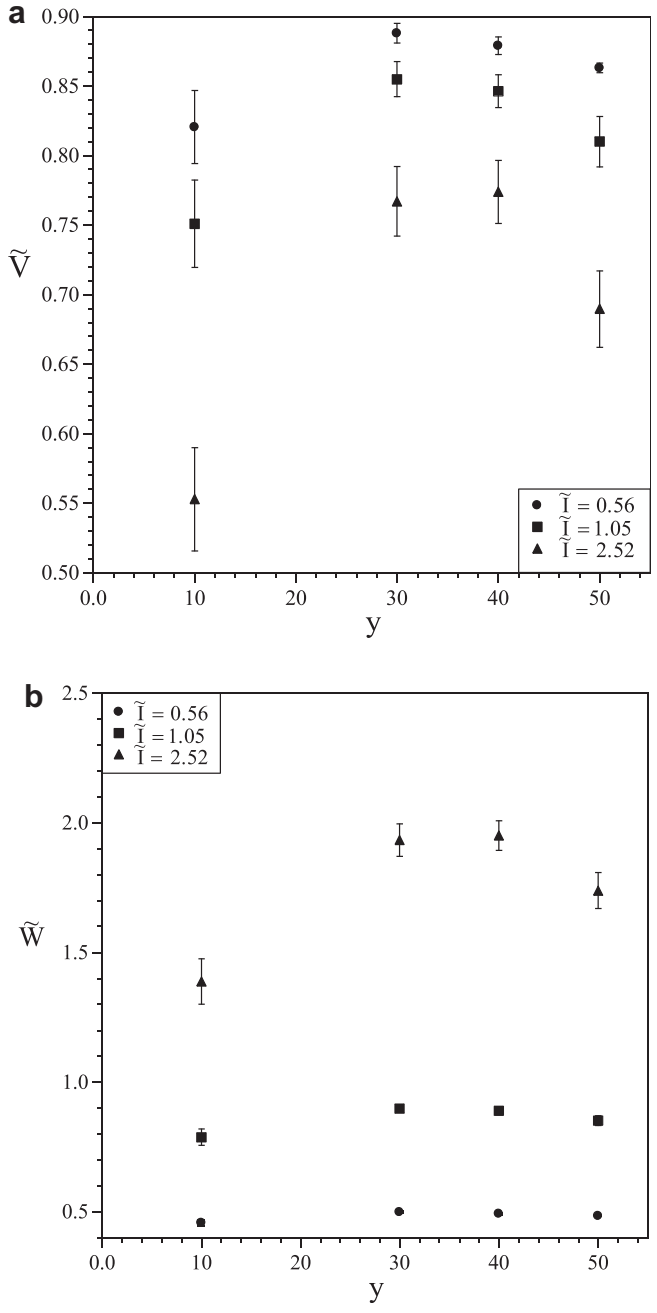


**Fig. 6.** Experimental AMFC potential (a) and power (b) output values as functions of KOH mass fraction for three current levels ($\tilde{I} = 0.56, 1.05$ and $2.52$).

to the AMFC mathematical model, i.e., temperatures and pressures, and then computing AMFC potentials and net power for the entire current operating range ($0 \le \tilde{I} \le \tilde{I}_{max}$). The input parameters are the geometric features and physical properties of the single AMFC. The geometry and several physical properties were measured directly from the AMFC prototype, and are listed in Table 2. The remaining necessary data were taken from the technical literature [1,14,26,28,29,36–40]. The reference case (geometry and properties) for all simulations in this study is the AMFC prototype.

The current ($I$) is considered an independent variable in the numerical simulation. The fuel cell electrical and net power were computed by starting from open circuit ($\tilde{I} = 0$), and proceeding with current increments ($\Delta\tilde{I} = 0.1$) until the electrical current reached the values experimentally obtained with AMFC prototype.

As pointed out earlier in the text, the model experimental validation was performed using 5 (five) different sets of measured data obtained with different KOH mass fraction in the electrolyte solution (10 wt. % , 20 wt. % , 30 wt. % , 40 wt. % and 50 wt. % ). There are some parameters that change with solution concentration ($k_{sol}, \rho_{sol}$ and $\sigma_{sol}$) and the appropriate values were taken from the literature [38,39] and are shown in Table 3. For clarity, the geometry of the AMFC prototype used in the experiments is summarized in Table 4. The model experimental validation initial step was to perform the model adjustment.

The model adjustment procedure consisted of solving the inverse problem of parameters estimation (IPPE) [41], using the mathematical model, i.e., by turning a variable into a parameter, and vice-versa. For that, what was originally a variable is imposed to the model as an input parameter. In this study, the variables available from the experiments were the measured voltage and current output of the AMFC prototype. Therefore, two parameters could become variables in the model. The procedure started by selecting the parameters to become the variables to be determined. The anode and cathode exchange current densities were selected due to their expected dependency on electrolyte solution concentration, which was the parameter that was experimentally varied. The exchange current density determines the magnitude of the oxidation and reduction reactions that occur in the electrodes at the equilibrium potential. Even though the net current is zero at equilibrium, balanced faradaic activity happens, and is expressed in terms of exchange current density [30,31] as follows:

$$i_0 = nFk^0 C_R^{\alpha} C_O^{(1-\alpha)} \tag{35}$$

where $k^0$ is the standard rate constant, and $C_O$ and $C_R$ the concentration of oxidized and reduced states respectively.

**Table 2**
Physical properties used as reference case in the numerical solution.

| | |
|---|---|
| $B = 0.156$ [42] | $R_f = 4.157$ kJ kg$^{-1}$ K$^{-1}$ |
| $c_{p,f} = 14.307$ kJ kg$^{-1}$ K$^{-1}$ | $R_{ox} = 0.2598$ kJ kg$^{-1}$ K$^{-1}$ |
| $c_{p,ox} = 0.918$ kJ kg$^{-1}$ K$^{-1}$ | $t_{ref} = 10^{-3}$ s |
| $c_{v,f} = 10.183$ kJ kg$^{-1}$ K$^{-1}$ | $T_f$, $T_{ox}$, $T\infty = 298.15$ K |
| $c_{v,ox} = 0.658$ kJ kg$^{-1}$ K$^{-1}$ | $U_{wi} = 50$ W m$^{-2}$ K$^{-1}$, i = 1 to 7 |
| $I_{ref} = 1$ A | $V_{ref} = 1$ V |
| $k_f = 0.182$ W m$^{-1}$ K$^{-1}$ | $\alpha_a$, $\alpha_c = 0.5$ |
| $k_{ox} = 0.0267$ W m$^{-1}$ K$^{-1}$ | $\zeta_1$, $\zeta_7 = 2$ |
| $k_p = 0.1298$ W m$^{-1}$ K$^{-1}$ | $\mu_1 = 8.96 \times 10^{-6}$ Pa s |
| ks,a = ks, $c = 0.1$ W m$^{-1}$ K$^{-1}$ | |
| $k_{sol} = 0.571$ W m$^{-1}$ K$^{-1}$ | $\mu_7 = 20.7 \times 10^{-6}$ Pa s |
| $K_2$, $K_6 = 4.2 \times 10^{-14}$ m$^2$ [14] | $\sigma_{sol} = 53.2\ \Omega^{-1}$ m$^{-1}$ |
| $K_3$, $K_5 = 4.2 \times 10^{-16}$ m$^2$ [14] | $\sigma_1$, $\sigma_7 = 1.5 \times 10^7\ \Omega^{-1}$ m$^{-1}$ |
| $p_f = 0.127$ MPa | $\sigma_2$, $\sigma_6 = 8570\ \Omega^{-1}$ m$^{-1}$ |
| $p_{ox} = 0.134$ MPa | $\phi_2$, $\phi_6 = 0.0085$ |
| $p\infty = 0.1$ MPa | $\phi_3$, $\phi_5 = 0.172$ |
| $q = 2.5$ | $\phi_4 = 0.71$ |

**Table 3**
Concentration-dependent parameters.

| $y$ | 10 wt.% | 40 wt.% | 50 wt.% |
|---|---|---|---|
| $k_{sol}$ | 0.61 | 0.57 | 0.60 |
| $\rho_{sol}$ | 1040.84 | 1406.39 | 1532.69 |
| $\sigma_{sol}$ | 20.08 | 53.22 | 47.61 |
| $i_{0,a}$ | 0.0021 | 0.0058 | 0.0046 |
| $i_{0,c}$ | 0.0002 | 0.0019 | 0.0005 |

**Table 4**
Geometry of the AMFC prototype of Fig. 1.

| | |
|---|---|
| $V_T = 2.5 \times 10^{-4} m^3$ | $\xi_3/\xi_x = \xi_5/\xi_x = 0.0058$ |
| $\xi_y/\xi_x = \xi_z/\xi_x = 3.95$ | $\xi_4/\xi_x = 0.0197$ |
| $\xi_1/\xi_x = \xi_7/\xi_x = 0.0789$ | $\xi_8/\xi_x = \xi_9/\xi_x = 0.3946$ |
| $\xi_2/\xi_x = \xi_6/\xi_x = 0.0108$ | $\xi_t/\xi_y = 0.02$ |
| | $\xi_c/\xi_y = 0.01$ |

Eq. (35) clearly shows that if the electrolyte solution concentration varies, new equilibrium conditions will be established, therefore a new exchange current density will result. Based on that, it is herein proposed to elaborate empirical correlations for the electrodes exchange current densities as functions of electrolyte solution concentration using 3 (three) data sets, corresponding to $y = 10$ wt. % , 40 wt. % and 50 wt. % . The numerical solution of the IPPE was obtained for the steady state at each current incremental value, and delivered exchange current values that showed a strong dependency on current for $0 \leq \tilde{I} \sim 1$, which stabilized in the range $1 \sim \tilde{I} \leq \tilde{I}_{max}$ for the 3 tested electrolyte solution concentrations. This effect indicates that it is reasonable to expect that the exchange current density for $1 \sim \tilde{I} \leq \tilde{I}_{max}$ could be empirically correlated as a function of the electrolyte solution concentration.

As a result, the AMFC prototype response was then numerically simulated using the stabilized values of exchange current densities shown in Table 3 for y = 10 wt. % , 40 wt. % and 50 wt. % . Fig. 7 shows in solid lines the numerically calculated potential curves for all tested electrolyte solution concentrations in the range $0 \leq \tilde{I} \leq \tilde{I}_{max}$, and the experimentally measured voltage and net power with error bars that were calculated with Eqs. (33) and (34). It is noted that the experimental uncertainties both for potential and power data were small for low currents, and increased as current increased. For $1 \sim \tilde{I} \leq \tilde{I}_{max}$, the numerical results lie within the error bars as expected, therefore with good qualitative and quantitative agreement with the experimental results. Regarding the power curves, there was good agreement both quantitatively and qualitatively between the simulation results and the experimental data. The numerical results remained within the error bars throughout

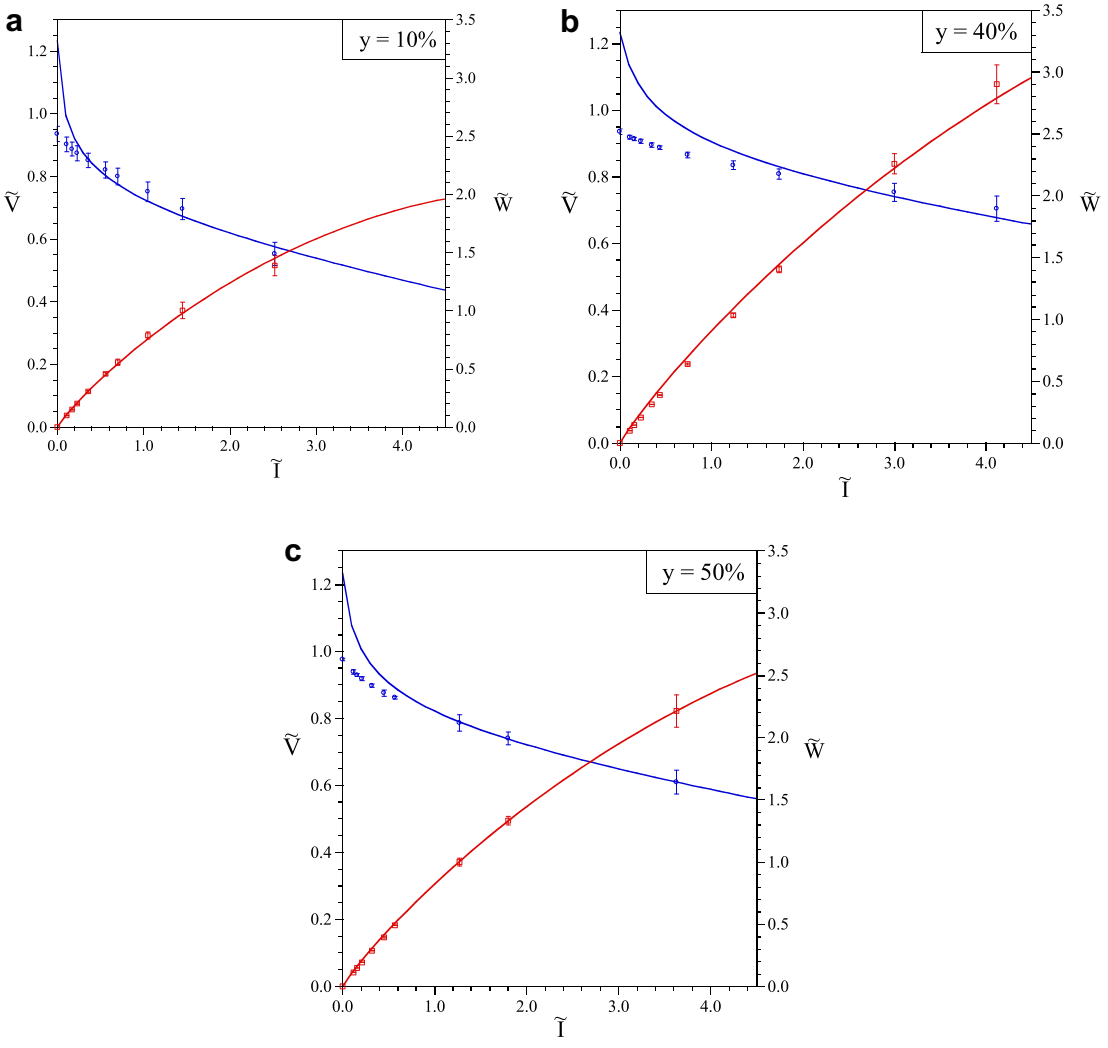


**Fig. 7.** Experimental model adjustment using y = 10 wt. % (a), 40 wt. % (b), and 50 wt. % (c).

the tested current range ($0 \leq \tilde{I} \leq 4.5$) and the maximum AMFC prototype measured power was $\tilde{W} \cong 3$.

The exchange current density defines the activity of the electrode and strongly influences the fuel cell performance. Using the 3 (three) ($i_{0,a}$, $i_{0,c}$) values of Table 3, the following empirical correlations were obtained for the electrodes used in the AMFC prototype shown in Fig. 1:

$$i_{0,a} = -2.14 \times 10^{-7} y^3 + 1.53 \times 10^{-5} y^2 - 0.00019\, y + 0.00272 \quad (36)$$

$$i_{0,c} = -4.35 \times 10^{-9} y^4 + 3.11 \times 10^{-7} y^3 - 5.16 \times 10^{-6} y^2 + 3.08 \times 10^{-5} y - 0.00014 \quad (37)$$

After performing the model adjustment, the next step was the model experimental validation. This task was achieved by using the remaining 2 (two) experimental data sets, i.e., the measured voltage and current obtained with $y = 20$ wt. % and 30 wt. % . Eqs. (36) and (37) were then used to determine ($i_{0,a}$, $i_{0,c}$) for y = 20 wt. % and 30 wt. % . The calculated ($i_{0,a}$, $i_{0,c}$) values were then used as input to the mathematical model in order to obtain numerically the AMFC prototype polarization and power curves. The numerically simulated AMFC response is shown in solid lines in Fig. 8 for $y = 20$ wt. % and 30 wt. % . The voltage curves lie within the error bars for $1 \sim \tilde{I} \leq \tilde{I}_{max}$, and the power curves for the entire tested range. Therefore, there was good agreement between numerical and experimental results with the use of the exchange current density empirical correlations, so that the model could be reliably used to simulate and analyze the AMFC response under different geometric and operating conditions for the range 10 wt.% $\leq y \leq$ 50 wt.%.

### 5.3. AMFC simulation

In order to illustrate the application of the experimentally validated AMFC mathematical model, numerical simulations are conducted for $y = 40$ wt.%, since it was shown experimentally that this is the optimal electrolyte solution for maximum AMFC net power output. Fig. 9 shows the resulting polarization and net power curves obtained with the simulation. The actual open circuit potential is equal to the reversible potential, because in the mathematical model it is assumed that there are no losses due to species crossover between the two electrodes and from internal currents. Therefore, with the model, it is possible to verify the contribution of anode and cathode potentials separately to the resulting total AMFC potential $\tilde{V}i$. As expected, cathode potential is smaller than anode potential.

Fig. 10 shows the AMFC internal temperature distribution. The temperature along the AMFC increases as current increases, since more heat is being generated by electrochemical reactions and potential losses (ohmic resistance and overpotentials - activation and diffusion). The CV5 shows a slightly higher temperature than CV3 because it is the control volume in which the oxygen reduction reaction takes place, which releases more heat than the hydrogen

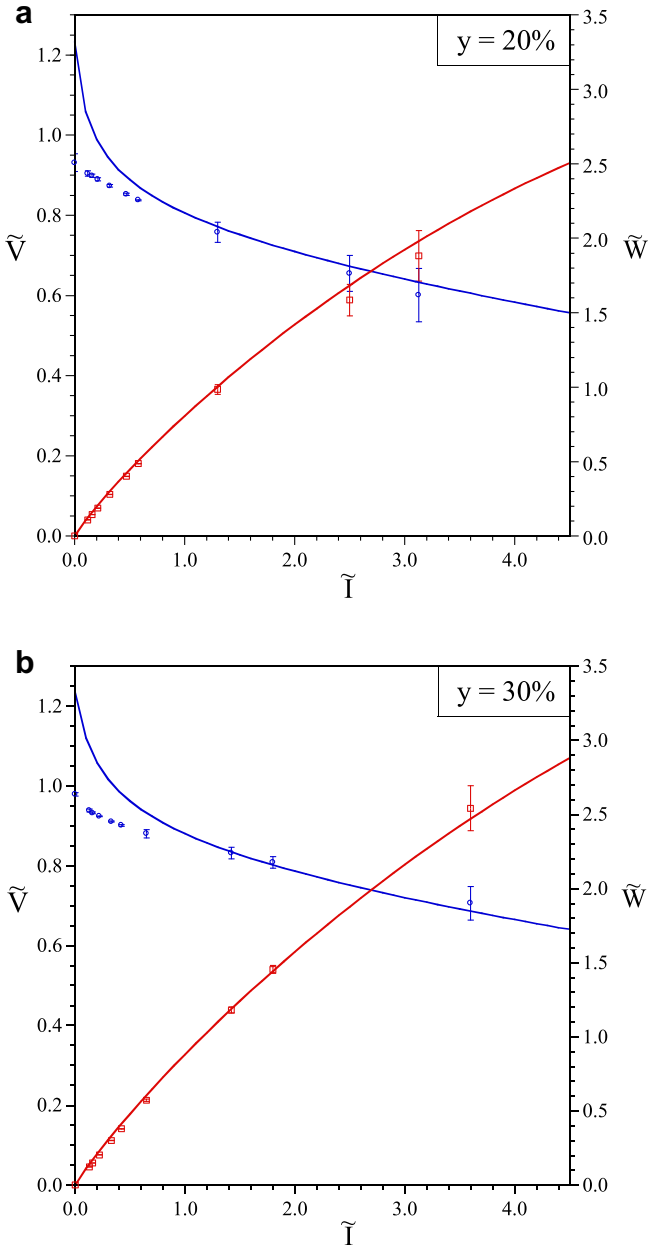


**Fig. 8.** Experimental model validation using y = 20 wt. % (a), and 30 wt. % (b).

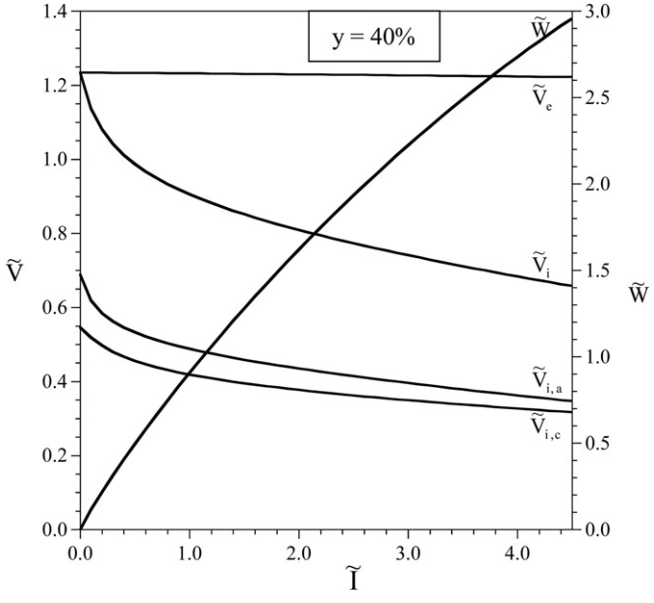


**Fig. 9.** The AMFC prototype polarization and power curves obtained numerically with the experimentally validated model for y = 40 wt. % .

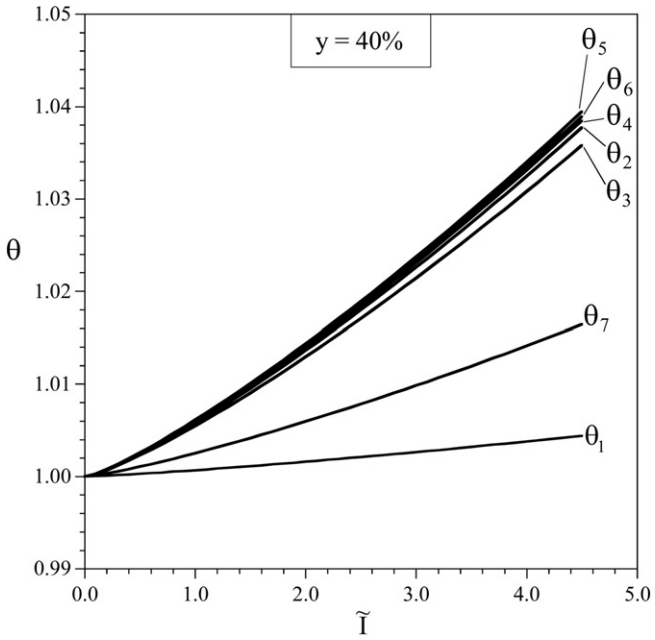


**Fig. 10.** The thermal response of the AMFC prototype obtained numerically with the experimentally validated model for y = 40 wt. % .

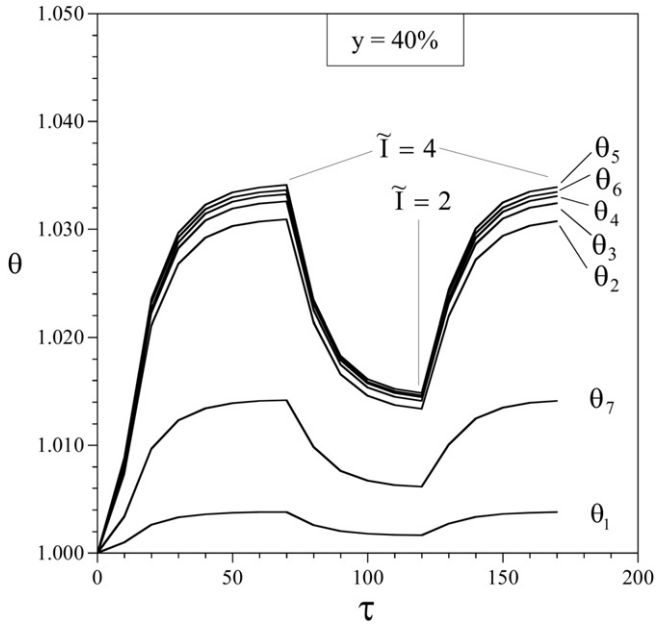


**Fig. 12.** The dynamic thermal response of the AMFC prototype according to changes in current load requirement obtained numerically with the experimentally validated model for y = 40 wt. % .

oxidation at CV3. These simulation results show that temperature varies considerably as fuel and oxidant flow across the cell during operation, therefore the commonly used uniform temperature assumption for fuel cell operation only holds for low current values. Such temperature spatial dependence is important to be considered in order to obtain representative AMFC power output values since exchange current densities and other parameters depend on temperature. Such temperature spatial dependency is expected to be more pronounced when a larger current interval is considered or for AMFC stack design.

The assessment of pressure drops in the gas channels (CV1 and CV7) allows for obtaining the actual value of output power produced by the AMFC via subtraction of the power required for pumping the fuel and the oxidant from the electrical power, as stated by Eq. (31). The simulation results of Fig. 11 show that CV7 pressure drop is higher than in CV1, since oxygen is roughly ten times more viscous than hydrogen. For low currents, pressure drops are small, since small fuel and oxidant mass flow rates are needed. However, as current increases, pumping power should not be neglected.

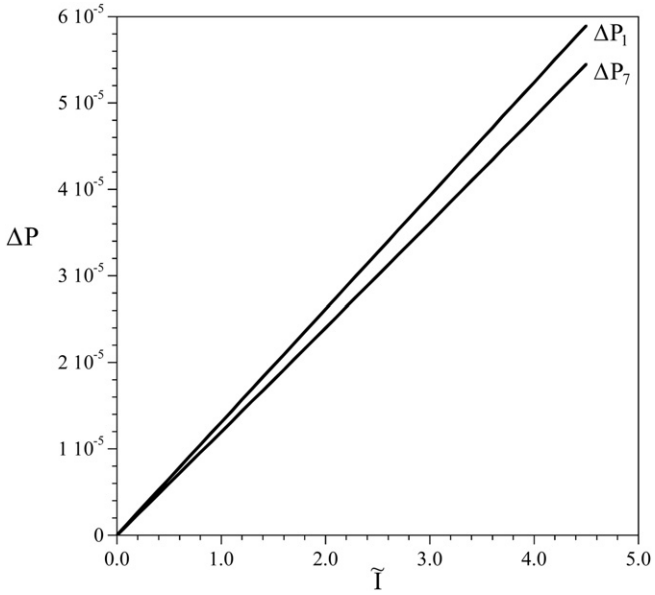


**Fig. 11.** The dimensionless pressure drops in the gas channels of the AMFC prototype obtained numerically with the experimentally validated model for y = 40 wt. % .

Finally, as an example of the model application in a transient simulation, a transient analysis is conducted numerically with the model. Fig. 12 shows the thermal transient response of the AMFC when the load current requirement changes from $\tilde{I} = 4$ to $\tilde{I} = 2$, then back to $\tilde{I} = 4$. Besides information on the time required to achieve new current levels, the results demonstrate that temperature varies significantly from one current level to another, an effect that becomes increasingly important as current increases, due to the increase in fuel cell heat generation at the reacting sites. Note also the temperature gradients within the cell, i.e., between the gas channels and membrane electrodes assembly. Such fuel cell operating temperature variation is commonly disregarded in most fuel cell studies found in the literature, normally under the assumption that the cooling system is capable of equilibrating fuel cell temperature at any desired setpoint independently of current, which is true only for the cooling channels, but not for the internal fuel cell components, as the present model demonstrates.

## 6. Conclusions

In this paper, an AMFC dynamic mathematical model with temperature dependence on space and current was introduced and experimentally validated by direct comparison with output voltage and power measurements performed in a cellulose-based AMFC prototype in the laboratory. The single AMFC voltage and power output were obtained numerically with the mathematical model, and the results show good qualitative and quantitative agreement with the measured experimental data. Appropriate dimensionless groups were identified to formulate the model, and the results presented in normalized charts for general application.

It is concluded from the experimental results that the startup transient is short and that there are optimal values of KOH mass fraction y ( ~40 wt. % ) which lead to maximum power, that are herein shown experimentally for the first time. The model was used to formulate empirical correlations for the exchange current density ($i_0$) in the electrodes with respect to the electrolyte concentration, and could be used for future AMFC development.

Temperature gradients along the fuel and oxidant flow path are shown to exist and increasingly more important as operating current increases, both in steady state or dynamic operation, mainly when the cell is subject to changes in operating current regime in time, which is a frequent demand in any fuel cell application. For AMFC stacks, significant temperature spatial gradients are also expected since large coolant flow rates are limited due to induced high pressure drops in the cooling channels, and should be taken into account in optimal AMFC stack design. Therefore, the obtained results demonstrate the importance of considering temperature dependence on space and current in AMFC mathematical models. The model presented in this paper accounts for temperature gradients in the flow direction and dependence on operating current. The model also considers the pressure drops in the gas channels, so that AMFC net power is computed for more realistic results. As a result, it is reasonable to state that the combination of accuracy and low computational time allow for the future utilization of the model as a reliable tool for AMFC simulation, control, design and optimization purposes.

## Acknowledgements

The authors acknowledge with gratitude the support of the Center for Advanced Power systems at Florida State University, AFOSR (Award No. FA9550-06-1-0527), the Brazilian National Council of Scientific and Technological Development, CNPq (projects 578066/2008-4 and 485651/2007-6), CAPES (projects 200/2007 and 2424/11-8), and the Mechanical Engineering Graduate Program (PGMEC) of the Federal University of Parana.

## References

[1] J.V.C. Vargas, A. Bejan, International Journal of Energy Research 28 (2004) 319–339.
[2] M.M. Mench, C. Wang, S.T. Thynell, International Journal of Transport Phenomena 3 (2001) 151–176.
[3] T. Burchardt, P. Gonerec, E. Sanchez-Cortezon, Z. Karichev, J.H. Miners, Fuel 81 (2002) 2151–2155.
[4] A. Tewari, V. Sambhy, M.U. Macdonald, A. Sen, J. Power Sources 153 (2006) 1–10.
[5] E. Gulzow, M. Schulze, J. Power Sources 127 (1–2) (2004) 243–251.
[6] E. Agel, J. Bouet, J.F. Fauvarque, J. Power Sources 101 (2001) 267–274.
[7] J.R. Varcoe, Phys. Chem. Chem. Phys. 9 (2007) 1479–1486.
[8] M. Cifrain, K.V. Kordesch, J. Power Sources 127 (2004) 234–242.
[9] L.M. Appelman, W.F. ten Barge, P.G.J. Reuzel, Am. Ind. Hyg. Assoc. J. 43 (1982) 662–665.
[10] American Industrial Hygiene Association (AIHA) in: Hygienic guide series. Anhydrous ammonia, Am Ind Hyg Assoc J 32 1971 139–142.
[11] S. Toyokun, S. Nagoya, J. Med. Sci. 71 (1–2) (2009) 1–10.
[12] J.V.C. Vargas, J.E.F.C. Gardolinski, J.C. Ordonez, R. Hovsapian, Alkaline Membrane Fuel Cell – Provisional Patent Application – US 61/363,689 filed on July 13, 2010.
[13] R. Souza, E.R. Gonzalez, Journal of Power Sources 147 (1–2) (2005) 32–45.
[14] L.S. Martins, J.E.F.C. Gardolinski, J.V.C. Vargas, J.C. Ordonez, S.C. Amico, M.M.C. Forte, Applied Thermal Engineering 29 (2009) 3036–3048.
[15] J.B. Young, Annu. Rev. Fluid Mech. 39 (2007) 193–215.
[16] L. Ma, D.B. Ingham, M. Pourkashanian, E. Carcadea, J. Fuel Cell Sci. Technol. 2 (2005) 246–257.
[17] I. Verhaert, M. Paepe, G. Mulder, Journal of Power Sources 193 (1) (2009) 233–240.
[18] M. Duerr, S. Gair, A. Cruden, J. McDonald, Journal of Power Sources 171 (2007) 1023–1032.
[19] S. Mohan, S.O.B. Shrestha, Journal of Fuel Cell Science and Technology 7 (4) (2010) 122–127.
[20] H. Weydahl, A.M. Svensson, S. Sundea, Journal of the Electrochemical Society 156 (3) (2009) A225–A237.
[21] R.K. Shah, A.L. London, Laminar Flow Forced Convection in Ducts, Supplement 1 to Advances in Heat Transfer, Academic Press, New York, 1978.
[22] A. Bejan, Convection Heat Transfer, second ed., Wiley, New York, 1995.
[23] R.B. Bird, W.E. Stewart, E.N. Lightfoot, Transport Phenomena, second ed. Wiley, New York, 2002.
[24] J.S. Newman, Electrochemical Systems, second ed., Prentice Hall, Englewood Cliffs, NJ, 1991.
[25] J.A. Wesselingh, P. Vonk, G. Kraaijeveld, Chemical Engineering Journal and the Biochemical Engineering Journal 57 (1995) 75–89.
[26] M.J. Moran, R. Shapiro, Fundamentals of Engineering Thermodynamics, third ed., Wiley, New York, 1993.
[27] W.L. Masterton, C.N. Hurley, Chemistry Principles & Reactions, third ed. Saunders College Publishing, Orlando, FL, 1997.
[28] R.H. Perry, D.W. Green, J.O. Maloney, Perry's Chemical Engineer's Handbook, sixth ed., McGraw-Hill, New York, 1984.
[29] A.A. Kulikovsky, J. Divisek, A.A. Kornyshev, Journal of The Electrochemical Society 147 (2000) 953–959.
[30] J.O.'M. Bockris, D.M. Drazic, Electro-chemical Science, Taylor and Francis, London, 1972.
[31] A.J. Bard, L.R. Faulkner, Electrochemical Methods – Fundamentals and Applications, second ed., Wiley, New York, 2001.
[32] D. Kincaid, W. Cheney, Numerical Analysis, Wadsworth, Belmont, CA, 1991.
[33] Editorial, ASME J. Heat Transfer 115 (1993) 5–6.
[34] S. Lipschutz, M.L. Lipson, Theory and Problems of Probability, second ed., McGraw-Hill, New York, 2000.
[35] H. Zhang, G. Lin, J. Chen, Energy 36 (2011) 4327–4332.
[36] F.P. Incropera, D.P. DeWitt, Fundamentals of Heat and Mass Transfer, seventh ed., Wiley, New York, 2011.
[37] F.B. Prinz, S.W. Cha, R.P. O'Hayre, W.G. Colella, Fuel Cell Fundamentals, second ed., Wiley, New York, 2006.
[38] W.D. Callister, Materials Science and Engineering: Introduction, seventh ed., Wiley, New York, 2007.
[39] R.J. Gilliam, J.W. Graydon, D.W. Kirk, S.J. Thorpe, International Journal of Hydrogen Energy 32 (2007) 359–364.
[40] I.D. Zait´s˘ev, G.G. Aseev, Properties of Aqueous Solutions of Electrolytes, CRC Press, Boca Raton, FL, 1992.
[41] W.J. Minkowycz, E.M. Sparrow, G.E. Schneider, R.H. Pletcher, Handbook of Numerical Heat Transfer, second ed., Wiley, New York, 2006, Chapter 17.
[42] M.R. Tarasevich, A. Sadkowski, E. Yeager, in: B.E. Convay, J.O.'M. Bockris, E. Yeager, S.U.M. Khan, R.E. White (Eds.), Comprehensive Treatise of Electrochemistry, 7, Plenum, New York, 1983, pp. 310–398.